UNIVERSITY OF CALIFORNIA SAN DIEGO

Surface Functionalization of Gold Nanoparticles and Peptide Design for Proteolytic Sensing in In Vitro Diagnostics

A Thesis submitted in partial satisfaction of the requirements
for the degree Master of Science

in

Bioengineering

by

Justin Wing Yeung

Committee in charge:

Professor Jesse Jokerst, Chair
Professor Ester Kwon, Co-Chair
Professor Xiaohua Huang

2023

The Thesis of Justin Yeung is approved, and it is acceptable in quality and form for publication on microfilm and electronically.

University of California San Diego

2023

DEDICATION

I dedicate this thesis to my Mom, Dad, and sister.

TABLE OF CONTENTS

LIST OF FIGURES

LIST OF TABLES

ACKNOWLEDGEMENTS

I would like to first, thank Dr. Jesse Jokerst for accepting me into the lab early on in my second year of my undergraduate program back in 2019. Despite having barely any research experience, he allowed me to work in his lab throughout my undergraduate and now, graduate degree and has helped foster my growth as a scientist.

I would also like to thank all the members of the Jokerst lab whom I have had the pleasure of working with in my four years in the lab. I have developed a plethora of skills working under many talented researchers and there is one person I want to thank in particular: Zhicheng Jin. He heavily impacted my development as a scientist and gave me the freedom to take on important roles in leading projects, which to my great satisfaction, has led to my own publishable work. I cannot express in words how thankful I am to have received his guidance and encouragement working in the Jokerst lab, and I could not have imagined becoming the scientist I am now without him.

Finally, I would like to acknowledge all my friends and family who have given me their unwavering support throughout all my hardships in academia. In particular, Angelique Wong and Annika Dang have been truly irreplaceable throughout my academic career and have always believed in my success, in spite of my own disbelief at times. I know for a fact that I would not be where I am today without them, and for that, I am forever grateful.

Chapter 1, in full, is a reprint of the material as it appears in American Chemical Society in Applied Materials & Interfaces 2023. Jin, Zhicheng; Yeung, Justin; Zhou, Jiajing; Retout, Maurice; Yim, Wonjun; Fatjová; Gosselin, Bryan; Jabin, Ivan; Bruylants, Gilles; Mattoussi, Hedi; O'Donoghue, Anthony; Jokerst, Jesse. The thesis author was a primary investigator and author of this paper.

Chapter 2, in full, has been submitted for publication as it may appear in Royal Society of Chemistry in Analyst 2023. Yeung, Justin; Jin, Zhicheng; Ling, Chuxuan; Retout, Maurice; Barbosa da Silva, Elany; Damani, Manan; Chang, Yu-Ci; Yim, Wonjun; O'Donoghue, Anthony; Jokerst, Jesse. The thesis author was the primary investigator and author of this paper.

VITA

2019 - 2022	Undergraduate Researcher, Jokerst Lab University of California San Diego
2022	Bachelor of Science in Bioengineering: Biotechnology University of California San Diego
2022 – 2023	Graduate Researcher, Jokerst Lab University of California San Diego
2023	Master of Science in Bioengineering University of California San Diego

PUBLICATIONS

Yeung, J. "Surface Functionalization of Gold Nanoparticles and Peptide Design for Proteolytic Sensing in In Vitro Diagnostics."

Yeung, J., Jin, Z., Ling, C., Retout, M., Barbosa Da Silva, E., Damani, M., Chang, Y.-C., Yim, W., O'Donoghue, A. J., Jokerst, J. V. "An Approach to Zwitterionic Peptide Design for Colorimetric Detection of the Southampton Norovirus SV3CP Protease." *In review.*

Jin, Z.*, **Yeung, J.***, Zhou, J., Retout, M., Fatjová, P., Gosselin, B., Jabin, I., Bruylants, G., Matoussi, H., O'Donoghue, A. J., Jokerst, J. V. "Empirical Optimization of Peptide Sequence and Nanoparticle Colloidal Stability: The Impact of Surface Ligands and Implications for Colorimetric Sensing." *ACS Applied Material & Interfaces*, 2023. 15(16): p. 20483–20494. *These authors contributed equally.

Jin, Z.*, Li, Y.*, Li, K., Zhou, J., **Yeung, J.**, Ling, C., Yim, W., He, T., Cheng, Y., Xu, M., Creyer, M. N., Chang, Y.-C., Fatjová, P., Retout, M., Qi, B., Li, S., O'Donoghue, A. J., Jokerst, J. V. "Peptide Amphiphile Mediated Co-assembly for Nanoplasmonic Sensing." *Angewandte Chemie*, 2023. 135(4): p. e202214394. *These authors contributed equally.

Chang, Y.-C.*, Jin, Z.*, Li, K., Zhou, J., Yim, W., **Yeung, J.**, Cheng, Y., Retout, M., Creyer, M. N., Fatjová, P., He, T., Chen, X., O'Donoghue, A. J., Jokerst, J. V. "Peptide valence-induced breaks in plasmonic coupling." *Chemical Science*, 2023. 14: p.2659-2668. *These authors contributed equally.

Yim, W., Zhou, J., Sasi, L., Zhao, J., **Yeung, J.**, Cheng, Y., Jin., Z., Johnson, W., Xu, M., Palma-Chavez, P., Fu, L., Qi, B., Retout, M., Shah, N. J., Bae, J., Jokerst, J. V. "3D-

Bioprinted Phantom with Human Skin Phototypes for Biomedical Optics." *Advanced Materials*, 2023. 35(3): p. 2206385

Jin, Z.*, Ling, C.*, Li, Y., Zhou, J., Li, K., Yim, W., **Yeung, J.**, Chang, Y.-C., He, T., Cheng, Y., Fatjová, P., Retout, M., O'Donoghue, A. J., Jokerst, J. V. "Spacer Matters: All-Peptide-Based Ligand for Promoting Interfacial Proteolysis and Plasmonic Coupling." *Nano Letters*, 2022. 22(22): p. 8932-8940. *These authors contributed equally.

Jin, Z.*, **Yeung, J.***, Zhou, J., Cheng, Y., Li, Y., Mantri, Y., He, T., Yim, W., Xu, M., Wu, Z., Fatjová, P., Creyer, M. N., Moore, C., Fu, L., Penny, W. F., O'Donoghue, A. J., Jokerst, J. V. "Peptidic Sulfhydryl for Interfacing Nanocrystals and Subsequent Sensing of SARS-CoV-2 Protease." *Chemistry of Materials*, 2022. 34(3): p. 1259-1268. *These authors contributed equally.

ABSTRACT OF THE THESIS

Surface Functionalization of Gold Nanoparticles and Peptide Design for Proteolytic Sensing in In Vitro Diagnostics

by

Justin Wing Yeung

Master of Science in Bioengineering

University of California San Diego, 2023

Professor Jesse Jokerst, Chair
Professor Ester Kwon, Co-Chair

Gold nanoparticles (AuNPs) have gained popularity in the development of *in vitro* diagnostics for their distinct physical and optical properties. More specifically, the surface plasmon resonance (LSPR) can be exploited via aggregation to generate a significant absorption band shift in the visible region of the electromagnetic spectrum, resulting in a pronounced red-to-blue color change that is visible to the naked eye. Our group has developed an intuitive and accessible, label-free diagnostic platform that takes advantage of the key

proteolysis step in viral replication by designing cleavable peptide intermediates to interface with gold nano colloids. Peptides are an effective probe due to their diverse and tunable functional groups found on amino acid side chains, which can interact with AuNPs through electrostatic, dithiol bridging, or amphiphilic interactions to promote aggregation. First, we determine the effects of modifying AuNPs with various surface ligands on aggregation propensity in the presence of charged, thiolate, or aromatic amino acids. The characterization study will then inform a final peptide design that encompasses all three molecular interactions which will be used to colorimetrically detect the coronavirus main protease. Second, we build on a well-established zwitterionic peptide design for electrostatically interfacing negatively charged AuNPs by providing additional optimizations of peptide design through the addition of lysine to arginine groups. An optimized peptide probe is then used to colorimetrically detect the norovirus main protease, additionally demonstrating the generalizability of this diagnostic platform.

CHAPTER 1

An Empirical Optimization of Peptide Sequence and Nanoparticle Colloidal Stability: The Impact of Surface Ligands and Implications for Colorimetric Sensing

Zhicheng Jin,[a,†] Justin Yeung,[b,†] Jiajing Zhou,[a] Maurice Retout,[a] Wonjun Yim,[c] Pavla Fajtová,[d] Bryan Gosselin,[e,f] Ivan Jabin,[e] Gilles Bruylants,[f] Hedi Mattoussi,[g] Anthony J. O'Donoghue,[d] and Jesse V. Jokerst[a,c,h]*

[†] These authors contributed equally

[a]Department of NanoEngineering, University of California, San Diego, La Jolla, CA 92093, United States

[b]Department of Bioengineering, University of California San Diego, La Jolla, CA 92093, United States

[c]Materials Science and Engineering Program, University of California, San Diego, La Jolla, CA 92093, United States

[d]Skaggs School of Pharmacy and Pharmaceutical Sciences, University of California, San Diego, La Jolla, CA 92093, United States

[e]Laboratoire de Chimie Organique, Université libre de Bruxelles (ULB), avenue F. D. Roosevel 50, CP160/06, B-1050 Brussels, Belgium

[f]Engineering of Molecular NanoSystems, Ecole Polytechnique de Bruxelles, Université libre de Bruxelles (ULB), avenue F. D. Roosevelt 50, CP165/64, B-1050 Brussels, Belgium

[g]Department of Chemistry and Biochemistry, Florida State University, Tallahassee, FL 32306, United States

[h]Department of Radiology, University of California, San Diego, La Jolla, CA 92093, United States

Abstract

Surface ligands play a critical role in controlling and defining the properties of colloidal nanocrystals. These aspects have been exploited to design nanoparticle aggregation-based colorimetric sensors. Here, we coated 13-nm gold nanoparticles (AuNPs) with a large library of ligands (e.g., from labile monodentate monomers to multicoordinating macromolecules) and evaluated their aggregation propensity in the presence of three peptides containing charged, thiolate, or aromatic amino acids. Our results show that AuNPs coated with the polyphenols and sulfonated phosphine ligands were good choices for electrostatic-based aggregation. AuNPs capped with citrate and the labile-binding polymers worked well for dithiol-bridging and π-π stacking-induced aggregation. In the example of electrostatic-based assays, we stress that the good sensing performance requires aggregating peptides of low charge valence paired with charged NPs of weak stability or vice versa. We then present a modular peptide containing versatile aggregating residues to agglomerate a variety of ligated AuNPs for colorimetric detection of the coronavirus main protease. Enzymatic cleavage liberates the peptide segment, which in turn triggers NP agglomeration and thus rapid color changes in < 10 min. The protease detection limit is 2.5 nM.

1.1 Introduction

The aggregation of metallic colloids leads to a bathochromic shift in their surface plasmon resonance (SPR) band and results in a pronounced color change.[1, 2] The ultimate color formation is a function of the core composition,[3] particle morphology,[4-6] and surface chemistry,[7, 8] which modulate the resonant coupling of light and free electrons in metallic nanostructures. For instance, the aggregation of gold nanoparticles (AuNPs) dramatically changes the dispersion color visually from red to purple/blue by naked eye due to the strong sensitivity of SPR to the interparticle distance combined with the high molar absorption coefficients.[9, 10] Such aggregation-induced plasmonic coupling has been exploited as an optical signal transduction strategy in colorimetric sensors with widespread use in bioanalytical applications.[11-14]

The realization of plasmonic coupling broadly demands either chemical linking (e.g., S-Au bond,[15, 16] conjugation,[17] recognition interactions,[18, 19] etc.) or changes in the environment (e.g., ionic strength,[20] solvent polarity,[21] ligand hydrophilicity,[22] etc.). Over the past two years, our group has designed a set of colorimetric sensors to study proteases through an array of NP types, proteases, and aggregation mechanisms. [5, 6, 15, 23-26] However, we have not yet systematically investigated the effects of surface chemistry. Surface chemistry plays a critical role in endowing the colloidal stability and interfacial functionality—these factors determine how nanoparticles adapt to the chemical or environmental stimuli and thus manifest in interparticle crosslinking and colorimetric sensing.[2, 27-29] The depth and diversity of the ligand field provides choices spanning from metal complexes,[30] small organic compounds,[8, 27] polymers,[31, 32] and other biomacromolecules (e.g., peptides,[15, 24, 33] proteins,[34] oligonucleotides[18]). These can tailor the versatile interfaces between nanoparticles and biological systems. Modifying surfaces with ligands allows to tune interparticle interactions, such as the Coulombic and

hydrophobic interactions, hydrogen and covalent bonds, or combinations thereof.[2, 8] Clearly, it is beneficial to screen the optimally-desired ligands to improve the performance of aggregation-based sensors and explain the diverse interactions between NPs and aggregants.

Here, citrate-AuNPs were first derivatized with a library of 19 ligands ranging from labile molecules to multicoordinating macromolecules, thus yielding NPs with varying physiochemical properties. The colloidal stability and color changes initiated by favorable electrostatic, covalent, and hydrophobic conditions were then evaluated using NaCl and dithiothreitol (DTT), and amphiphilic peptide solutions. Our results showed that the surface ligand plays a critical role in defining the critical coagulation concentration (CCC), aggregation mechanism, and color patterns. Consequently, this allowed us to screen the optimal NP coating and rationally develop a versatile peptide that contained charged, thiolate-presenting, and aromatic amino acid residues (i.e., Arg, Cys, Phe) that rapidly induce colorimetric signals. We finally validated the sensing performance targeting SARS-CoV-2 main protease with a detection limit at 2.5 nM and demonstrated its good performance in complex matrices including saliva. The results can facilitate new NP modifications for plasmonic sensing.

1.2 Results and Discussion

Rationale

Evaluating the effects of surface chemistry on NP aggregation-based colorimetric sensors was motivated by the desire to improve their performance, e.g., working window, sensitivity, etc. A second goal was to provide better understand the diverse interplays between NPs and aggregants (here, peptides). This was also inspired by our experimental observations relating to the different aggregation propensity of several NPs in the presence of the same aggregating

peptide.[15] The Derjaguin–Landau–Verwey–Overbeek (DLVO) theory stresses the balance of the van der Waals attractive force and electrostatic repulsive force on colloidal stability.[35] Thus, NPs are more likely to aggregate upon reduction of the double-layer repulsion by (i) adding oppositely charged peptides and/or (ii) decreasing the surface potential. The latter is directly related to the surface chemistry and thus impacts coagulation between NPs and peptides via electrostatic interactions.

Covalent dithiol-bridging and non-covalent π-π stacking can also facilitate AuNP coagulation.[16, 35-37] Typically, color changes prevail for AuNPs of compact ligand layers and in favorable particle-particle interacting environments.[27, 28] Meanwhile, minimal or no optical change is observed for AuNPs capped by inert, entropic, and strong-coordinating ligands.[32, 38, 39] In this study, the effect of surface ligands on colorimetric assays was investigated using 19 ligand-metal nanocomposites comprising of 13-nm AuNPs. Aggregation was evaluated using a protease-cleavable peptide that is flanked by segments with Arg, Cys, and Phe amino acids, as shown in Figure 1.1a (see TEM in Figure S1.1). Figure 1.1b shows the chemical structures of the ligands included here. These molecules represent different molecular weights, charges (neutral or anionic for the compatibility with citrate-AuNPs), and coordination strengths, thus evaluating a wide range of colloidal stability on nanoparticles.[8]

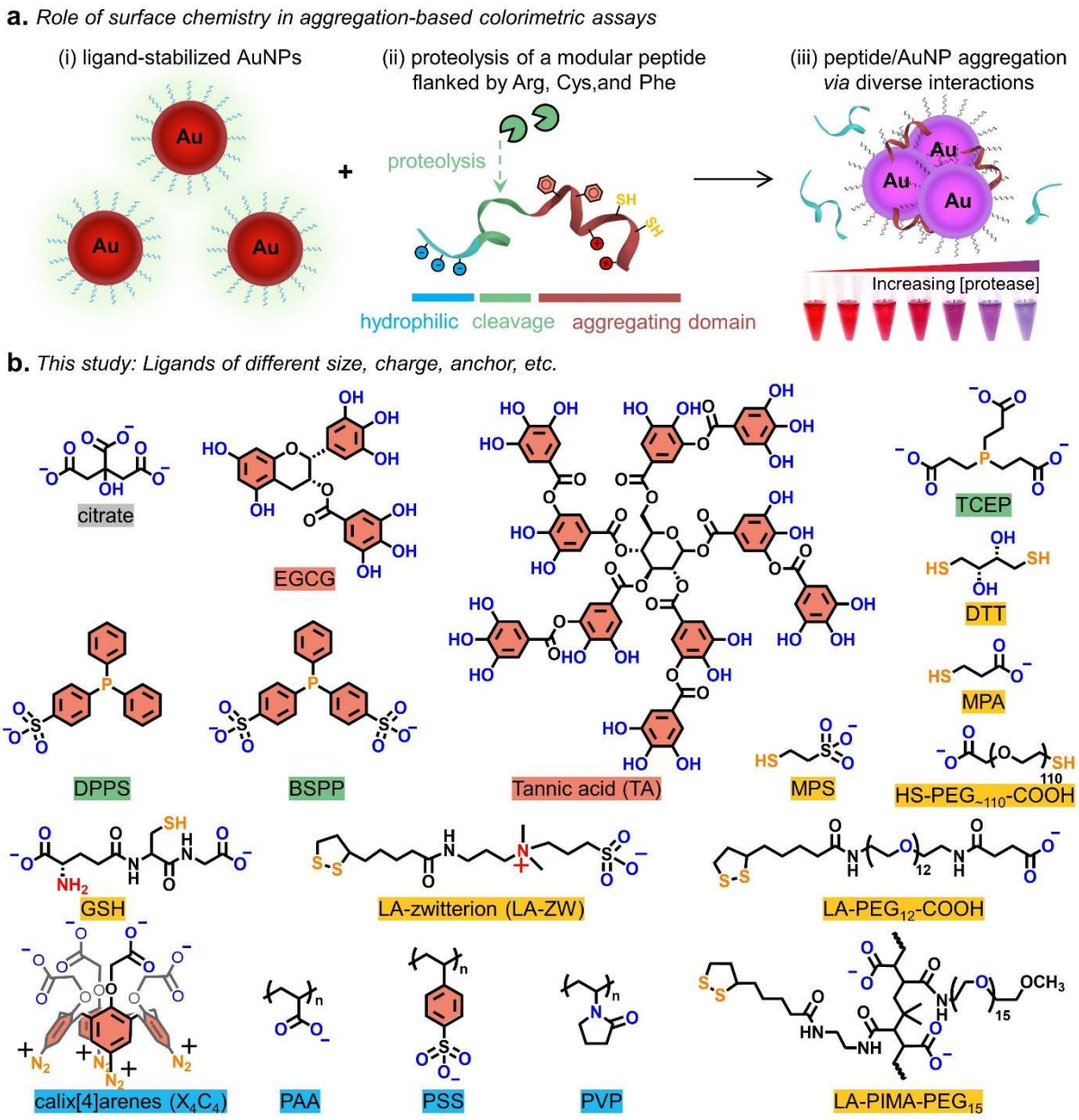

Figure 1.1 (a) Thematic illustration of how surface ligands on AuNPs trigger aggregation following incubation with proteolytically-cleaved peptide where the Arg, Phe, and/or Cys amino acids in the peptide segments promote interparticle association via charge neutralization, π-π stacking, or disulfide-bridge formation, respectively. This leads to pronounced color changes as a function of protease concentration [see the inset in part (iii)]. **(b)** Structure of the ligands used in this study including polyphenols (names on red), phosphine (green), thiolate (yellow), and other macromolecular ligands (blue). Note that the aryldiazonium groups in calix[4]arene (X_4C_4) are reduced in aryl radicals that form Au-C bonds with the gold surface.[40] BSA structure is not included. In the chemical structures, the solubilizing block is coded in blue/red atoms and the anchoring group is coded in yellow/blue atoms.

Ligand library and characterization of AuNPs

Despite a combination of molecular forces involved in ligand-to-metal interactions, we simplified our discussion and grouped these ligands based on the Hard-Soft Acid-Base (HSAB) theory where the Au atom receptor on nanosurfaces is classified as a soft Lewis acid.[41] The hard base-type ligands have characteristic anchors such as hydroxyl, carboxylate (or carboxyl), and sulfonate groups, which are expected to be labile molecules and may weakly passivate Au nanosurfaces; examples here include citrate, polyphenols [i.e., (−)-epigallocatechin gallate (EGCG), tannic acid (TA)], and labile binding macromolecules [i.e., poly(acrylic acid) (PAA), poly(sodium 4-styrenesulfonate) (PSS), polyvinylpyrrolidone (PVP)].[42] The soft base type ligands tethered with thiol (Au−S strength ≈ 126−184 kJ/mol[43]), phosphine (Au−P strength ≈ 222 kJ/mol[44]), or carbon (Au−C strength ≈ 227 kJ/mol[45]) anchors are known for strongly coordinating on AuNPs and thus favoring colloidal stabilization; examples here include phosphine ligands [i.e., tris(2-carboxyethyl)phosphine (TCEP), (diphenylphosphino)benzene sulfonate (DPPS), bis(p-sulfonatophenyl)phenylphosphine (BSPP)], thiolate ligands [i.e., dithiothreitol (DTT), mercaptopropionic acid (MPA), mercaptopropane sulfonate (MPS), glutathione reduced (GSH), thiolate carboxyl-poly(ethylene glycol) (HS-PEG-COOH), lipoic acid-zwitterion (LA-ZW), lipoic acid-terminated carboxyl-poly(ethylene glycol) (LA-PEG-COOH), poly(isobutylene-alt-maleic anhydride) with LA and methoxy-PEG pendant groups (LA-PIMA-PEG)], and calix[4]arene (X_4C_4) molecules.[27, 29, 46, 47] The ligand exchange protocol starting from citrate-AuNPs was performed according to a previous report with slight modifications.[29, 39] Note that the MPS- and MPA-capped AuNPs were sequentially derived using BSPP-AuNPs as the intermediate. The X4C4 ligand is modified upon reduction and NP synthesis in situ without ligand exchange, and it is grafted through covalent Au-C bonds.[40] The new

ligand-capped AuNPs were characterized by dynamic light scattering (DLS) and zeta potential (ζ) measurements (Table 1.1). The larger hydrodynamic diameter (DH) and polydispersity index (PDI) measured after ligand substitution indicate the more complex architecture of the new coatings than native citrate anions.[48] These measured DH values are consistent with our previous data collected for AuNPs prepared using similar methods.[15]

Table 1.1. Hydrodynamic size (DH), zeta potential (ζ), and critical coagulation concentration (CCC)[a] for the various ligand-stabilized AuNPs. The DLS measurements were carried out in DI water. The CCC values quantify the colloidal stability in NaCl,[27, 49] dithiothreitol (DTT),[15, 50] and amphiphile peptide (FFPC) assays.[37] These assays screen for the favorable electrostatic, covalent, and π-π stacking interactions between the AuNPs and aggregants, respectively.

[a] The critical coagulation concentration is set as the first value corresponding to a sizable jump in the absorption ratio, as shown in **Figure 1.3**.
[b] "N.D." indicates aggregation Not Detected under the tested conditions.

Ligand type	Sample	D_H (nm)	PDI	Zeta ζ (mV)	NaCl Test (mM)	DTT Test (μM)	FFPC Test (μM)
Native	**Citrate-Au**	18.2	0.216	-30.4 ± 2.7	>50	2-100	>10
Polyphenols	**EGCG-Au**	24.4	0.207	-30.2 ± 1.7	>500	5-50	N.D. [b]
	TA-Au	21.0	0.270	-35.2 ± 2.9	>100	5-100	N.D.
Phosphine ligands	**TCEP-Au**	21.0	0.284	-34.9 ± 3.0	>500	2-20	>50
	DPPS-Au	18.2	0.182	-25.2 ± 0.3	>50	N.D.	N.D.
	BSPP-Au	18.2	0.223	-31.3 ± 1.8	>100	N.D.	N.D.
Thiolate ligands	**DTT-Au**	24.4	0.147	-41.8 ± 0.2	>50	N.D.	>200
	MPA-Au	21.0	0.168	-30.6 ± 1.0	>50	N.D.	N.D.
	MPS-Au	24.4	0.280	-46.1 ± 0.6	>50	N.D.	N.D.
	GSH-Au	18.4	0.053	-35.6 ± 2.7	>200	N.D.	N.D.
	HS-PEG$_{\sim 110}$-COOH-Au	24.4	0.048	-36.4 ± 3.8	N.D.	N.D.	N.D.
	LA-PEG$_{12}$-COOH-Au	21.0	0.194	-31.2 ± 1.7	N.D.	N.D.	N.D.
	LA-ZW-Au	21.0	0.117	-26.6 ± 1.8	N.D.	N.D.	N.D.
Macromolecular ligands	**X_4C_4-Au**	43.8	0.576	-31.6 ± 2.8	>200	N.D.	N.D.
	PAA-Au	37.8	0.162	-46.8 ± 0.4	>100	2-100	N.D.
	PSS-Au	21.0	0.423	-41.5 ± 0.7	>50	2-100	>10
	PVP-Au	24.4	0.044	-30.5 ± 0.6	N.D.	5-100	>20
	LA-PIMA-PEG$_{15}$-Au	28.2	0.225	-31.2 ± 1.7	N.D.	N.D.	N.D.
	BSA-Au	50.7	0.193	-24.3 ± 0.1	N.D.	N.D.	N.D.

The above size characterization for the derivatized AuNPs was further corroborated by gel electrophoresis (Figure 1.2) due to the sensitivity of the electrophoretic mobility to subtle changes in the surface charge and hydrodynamic dimension. The citrate- and DTT-AuNPs showed instant aggregation in the running buffer (pH 8.3) and thus had no mobility shift. Most of the other NPs were stable enough to travel towards the anode, a property attributed to the hydroxyl/carboxylate/sulfonate groups around the nanocrystal. For example, the polyphenol-, sulfonated phosphine- and thiolate ligands-capped AuNPs exhibited sharp and narrow gel bands, indicating a low size dispersity. The TCEP-AuNPs showed a significant band smear implying moderate colloidal stability—this result is consistent with other reports and ours.[15, 27] Meanwhile, AuNPs ligated with negatively-charged polymers such as LA-PEG-COOH (990 Da),[51] PAA (15 kDa), PSS (70 kDa), LA-PIMA-PEG (25 kDa),[48] and BSA (66 kDa) have retarded band shifts presumably due to the large size of the nanocomposites. A close look at the band of PAA-AuNPs and PSS-AuNPs indicates that these complexes were too large to travel in the gel pores and thus showed a long trailing tail.[15] The PVP (40 kDa)-AuNP band showed no movement due to its charge neutrality. The above observations confirmed that ligand exchange on AuNPs with various ligands took place, and the derivatized AuNPs have distinct properties such as charge, size, and stability.

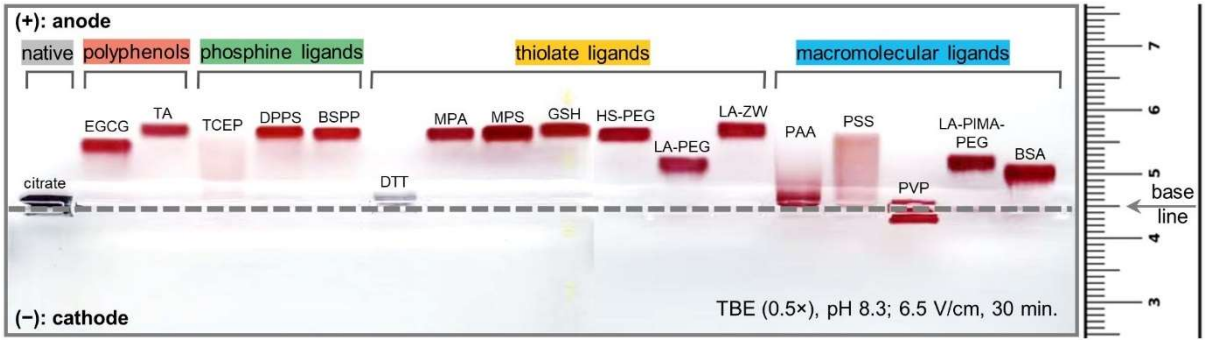

Figure 1.2. Agarose gel (0.7%) electrophoresis images collected from AuNPs capped with different ligands. Gel conditions are given on the bottom right, and the samples were prepared using a mixture of 3 μL glycerol and 47 μL AuNPs (10 nM). Note that tris-borate-EDTA buffer (TBE, 0.5×, pH 8.3) promotes instant aggregation of citrate- and DTT-capped AuNPs.

Colorimetric tests under excess ions, thiols, and aromatic moieties

Next, evolution of the dispersion color and colloidal stability of the ligand-stabilized AuNPs (3.4 nM, 100 μL) was evaluated in solutions containing NaCl (0 – 1 M),[27, 49] DTT (0 – 100 μM),[15, 50] and amphiphilic peptides (i.e., solubility of FFPC in water: 500 μM).[37] These assays screen for the favorable interparticle interactions (e.g., electrostatic, covalent, and π-π stacking[39, 49, 52]) imparted by each ligand coating, and thus have important implications in designing peptides or other substrates for aggregation-based colorimetric assays. When the colloidal stability is compromised, the red color turns to purple/blue and finally to grey corresponding to higher aggregation levels.

In the first assay, charged AuNPs collapse with high levels of counterions due to the shortened Debye length and reduced electrostatic double-layer potential as described by the Schulze-Hardy rule.[20, 35, 53] Figure 1.3a shows that NPs modified with compact and charged ligands, regardless of the anchoring groups, were prone to aggregation and showed color changes in high ionic strength conditions albeit at different thresholds of NaCl concentration.[27, 49] The quantitative assessment (i.e., ratio at Abs_{600}/Abs_{520}) is shown in Figure 1.3d, and the CCC

(defined as the first concentration of signal jump[54]) is summarized in Table 1.1. The clinically-relevant level for sodium is about 140 mM at which point citrate-, TA-, TCEP-, DTT-, MPA-, MPS-, and PSS-capped AuNPs showed color changes and thus may suffer from background interference in clinical samples. AuNPs protected by EGCG, DPPS, BSPP, GSH, X_4C_4, and PAA molecules were more resistant to the ionic environment and produced color changes only when the salt concentration exceeds 200 mM, thus implying that they are good candidates for electrostatic-induced plasmonic coupling. In comparison, ligands appended with PEG blocks or zwitterionic motifs are expectedly less sensitive to ionic strength and retained the colloidal stability of AuNPs throughout the tested conditions.[29] The zeta potential can provide valuable information for predicting colloidal stability during charge screening tests, but its value must be weighted relative to other factors such as ligand size and binding strength,[39, 49] which can also impact the CCC values as shown in Table 1.1.

Figure 1.3. (a-c) Color patterns of the ligated AuNPs (3.4 nM, 100 μL) in a series of NaCl, dithiothreitol (DTT), and amphiphilic peptide (FFPC) solutions of increasing concentrations (pH ~8.0). Shown are the cropped images at 10 min incubation. Red indicates dispersed nanoparticles. Purple, blue, and grey indicate increasing aggregation levels. The color pattern of DTT-AuNPs under DTT test is not included due to a low reproducibility. **(d-f)** Quantitative analysis of the color patterns by measuring the ratiometric absorbance, Abs_{600}/Abs_{520}. The critical coagulation concentration (CCC) is defined as the first point of signal jump, where the ratiometric absorbance may vary. Error bars = standard deviations (n = 3). Panel **b** is reprinted with permission from ref. 15. Copyright 2022 American Chemical Society.

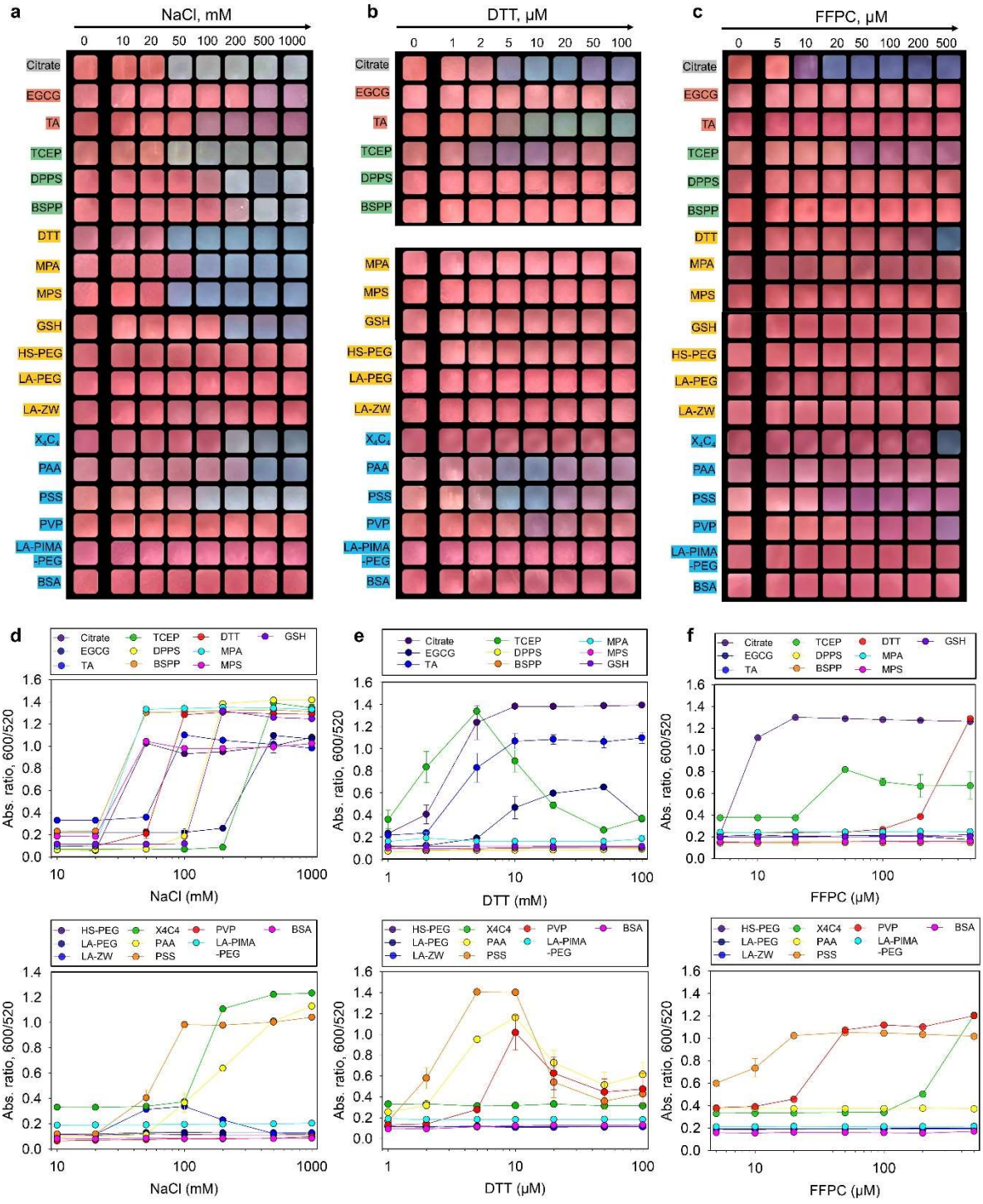
a
NaCl, mM
0 10 20 50 100 200 500 1000
b
DTT, μM
0 1 2 5 10 20 50 100
c
FFPC, μM
0 5 10 20 50 100 200 500
Citrate
EGCG
TA
TCEP
DPPS
BSPP
DTT
MPA
MPS
GSH
HS-PEG
LA-PEG
LA-ZW
X4C4
PAA
PSS
PVP
LA-PIMA -PEG
BSA
d
e
f
Abs. ratio, 600/520
NaCl (mM)
DTT (mM)
FFPC (μM)
NaCl (μM)
DTT (μM)
FFPC (μM)

In the second case, DTT molecules show high affinity to gold surfaces and competitively displace labile ligands, thus favoring chemical crosslinking and plasmonic coupling.[15, 50] The covalent aggregation is promoted in ionic conditions (i.e., 10 mM of NaCl) because of added screening effects; note that all the AuNPs were stable in 10 mM NaCl.[39] Figure 1.3b shows that citrate-, TA-, TCEP-, PAA-, and PSS-capped AuNPs (mostly hard Lewis base anchoring groups) agglomerated in the DTT test: These gold dispersions rapidly changed colors at low amounts of DTT (e.g., 5−20 μM), while the same nanoparticles were stabilized at high concentrations probably due to the replacement of the native ligands by DTT and saturation of the particle surfaces.[46]

The ratiometric absorbance data at various DTT concentrations for each AuNP type are summarized in Figure 1.3e and Table 1.1. The sulfonated phosphine (i.e., DPPS, BSPP)-coated AuNPs were resistant to DTT aggregation for hours, which may be attributed to the steric hindrance from the bulky aromatic rings that impedes ligand substitution. In addition, the nanoparticles functionalized with labile polymers (i.e., PAA and PSS) exhibited narrow aggregation windows (i.e., 5−10 μM). As expected, AuNPs modified with high densities of thiolate ligands were insensitive to the DTT assay.

In the third scenario, increasing interfacial hydrophobicity destabilizes nanoparticles in aqueous media via solvophobic interactions, thus promoting their self-assembly and plasmonic coupling.[37] The FFPC peptide is a unique, compact, and neutral amphiphile simultaneously exhibiting good water-solubility (from Pro),[24, 55] aromaticity (from Phe),[52] and surface affinity (from Cys).[37] The inclusion of the Cys sulfhydryl localizes aromatic interactions at bio-nano interfaces, which promotes mass-driven ligand exchange and AuNP aggregation in aqueous media. These unique properties make the FFPC peptide suitable for screening coatings that favor

color changes via π-π stacking. Citrate-, TCEP-, DTT-, X4C4-, and PSS-AuNPs aggregated in the solution of FFPC (Figure 1.3c). The corresponding CCC is shown in Figure 1.3f and Table 1.1. This result agrees well with the above DTT test assuming that both assays require competitive displacement of the native ligands to initiate particle aggregation. Surprisingly, X4C4-AuNPs stabilized by covalent Au-C bond showed dramatic particle agglomeration at 500 μM of FFPC peptide. It may be due to the fact that the X4C4 ligands are strongly grafted at the surface and thus could not reorganize as thiols in self-assembled monolayers, leaving some gold surface available for sequestering thiols. The FFPC peptide being longer than DTT, and it can protrude from the X4C4 layer and render the particle coating more hydrophobic, leading to their aggregation. Figures S3-5 detailed all the spectroscopic evolution of each AuNP sample in the above NaCl, DTT, and FFPC assays indicating a decrease in the SPR peak along with an increase in the absorbance at longer wavelengths.

Aggregation assays with peptides

Inspired by the above aggregation strategies, the charge/affinity/amphiphilicity of a specific substrate can be fine-tuned for colorimetric sensing of proteases where a diverse set of chemical functions provided by the aliphatic, protic, polar, aromatic amino acid side chains, and combinations thereof enable a versatile peptide library of distinct physicochemical properties. The selectivity is based on molecular recognition between the protease and the programmed peptide. Here, we selected SARS-CoV-2 M^{pro} to report on three sets of AuNP-aggregating peptide segments (see Figure 1.4 and Table 1.2); M^{pro} is known to effectively cleave at the C-terminal of Gln (Q) in the AVLQ↓SGF sequence.[56] The first peptide used electrostatic fragment (referred to as EF): two Arg (*R*) were positioned near the N-terminus for promoting electrostatic interactions, i.e., SGF*R*GG*R*GG.[23] The second peptide used thiolate fragment (referred to as TF),

two Cys (*C*) were coded to aggregate AuNPs via covalent bonding, i.e., SGFA*C*GAG*C*.[15] The third peptide used aromatic fragment (referred to as AF), two Phe (*F*) were incorporated to promote AuNP aggregation through π-π stacking interactions, i.e., SG*FF*PC.[52] Note that these peptide segments retain the SGF sequence to mimic the Mpro cleavage site, and contain a spacer sequence using Gly (G), Ala (A), and/or Pro (P).[24] The peptide synthesis has been confirmed by HPLC and ESI-MS data (Figure S1.6).

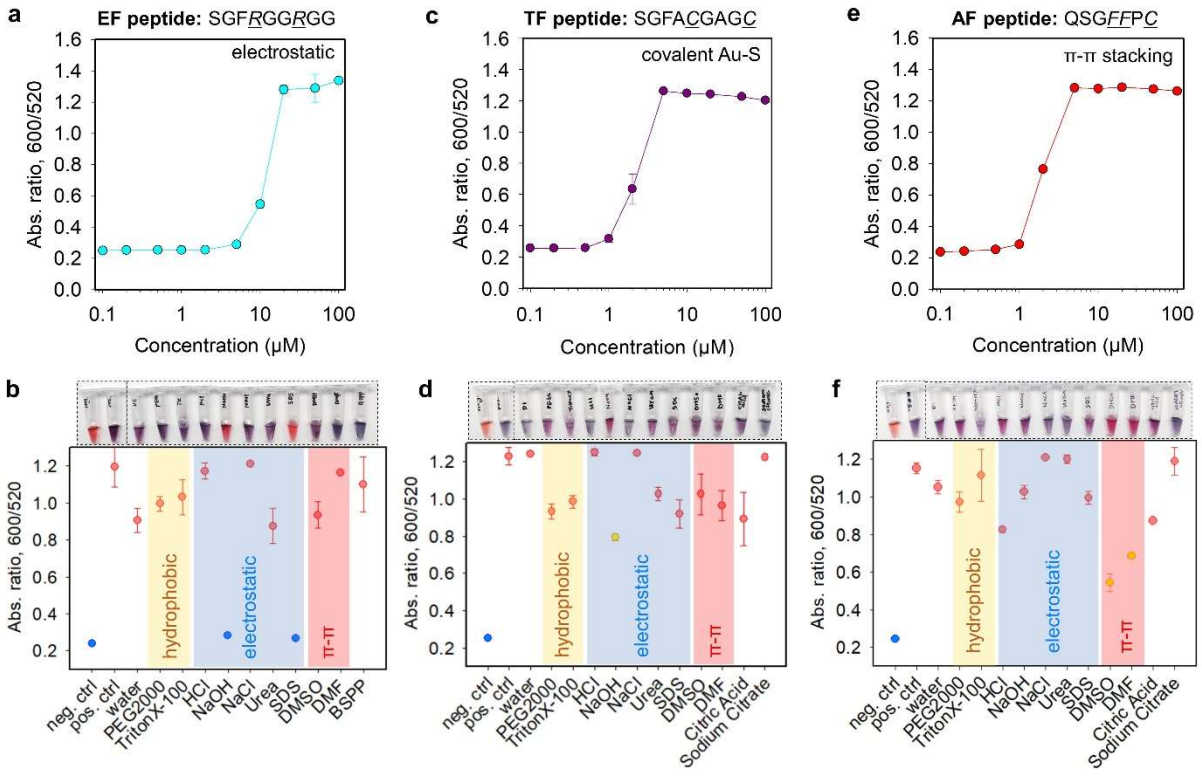

Figure 1.4. Aggregation titration of the representative paired **(a)** EF/BSPP-AuNPs, **(c)** TF/citrate-AuNPs, and **(e)** AF/citrate-AuNPs where the critical coagulation concentrations were determined to be about 10, 2, and 2 μM, respectively. EF = electrostatic fragment; TF = thiolate fragment; and AF = aromatic fragment. **(b, d, f)** White-light image (top) and quantified reversal color change (bottom) of the peptide/AuNP aggregates in different surfactant solutions (10 mM, 100 μL) or solvents (100 μL). Negative control used the AuNPs only, and positive control used the peptide/AuNP aggregates only. The yellow area indicates dominant hydrophobic interactions, the blue area indicates prevalent electrostatic interactions, and the red area implies strong π-π stacking forces. Error bars = standard deviations (n = 3).

Table 1.2. Peptide and segment information. The electrostatic fragment (EF), thiolate fragment (TF), and aromatic fragment (AF) could induce aggregation of the AuNPs *via* electrostatic, covalent, and π-π interactions, respectively. The Mega peptide after proteolysis can trigger AuNP aggregation *via* these multiple interactions.

Name	Sequence[a]	M. W. (g/mol)	Enzyme	Description
EF	SGF*R*GG*R*GG-Am	848.43	N/A	Two Arg, +2 charge
TF	SGFA*C*GAG*C*-Am	770.28	N/A	Two Cys, dithiol bridge
AF	SG*FF*PC-Am	655.28	N/A	Two Phe, aromatic moiety
Mega	DDDTSAVLQ↓SG*FFRCR*P*C*-Am	2014.90	M^{pro}	Zwitterionic, dithiolate, and aromatic substrate

[a] All peptides have a free N-terminus (*i.e.*, uncharged -NH_2 at pH 8.0) and an amidated C-terminus (*i.e.*, -Am). ↓ designates the M^{pro} cleavage site.

Next, the 19 types of ligated AuNPs were titrated with 0 to 100 μM of the above peptide segments, and the representative time-dependent aggregation kinetics are shown in Figure S1.7. The results at 10 min readout time were analyzed to pursue a rapid detection (Figure S1.8). The types of ligated AuNPs aggregated by the EF, TF, and AF peptide agree with the results from the above NaCl, DTT, and FFPC tests. This is because the peptides were customized to mimic the properties of these simple chemicals and thus the same interplay between the coating and peptide segment.

The Arg-rich EF segment agglomerated AuNPs coated with citrate, polyphenols, phosphine, DTT, MPA, MPS, X4C4, PAA and PSS ligand. The charge-based aggregation depends on two aspects: (i) charge valence (Z) of counterions that follows by the Schulz-Hardy rule, and (ii) colloidal stability that follows the DLVO theory.[35]

In the first aspect of electrostatic based aggregation, the corresponding CCC values for each ligated AuNP with EF peptide are at four orders of magnitude lower than that with NaCl (i.e., observed 10,000-fold less, see Tables 1 versus 3). This discrepancy broadly follows the

Schulz-Hardy rule (i.e., CCC ∝ Z6, theoretically 64-fold less), where the charge valence in an EF segment is twice as higher as a simple Na+ and thus less EF is required to electrostatically attract oppositely charged NPs. The different observed and theoretical values could result from the distinct ion geometries for different ions of the same valence,[57] e.g., Arg guanidinium allows interactions in three possible directions with the anionic counterparts through its three asymmetrical nitrogen atoms, compared to the Na+. On the one hand, these findings imply that the Arg-rich EF segment could be derived to other substrates with positively charged side chains (e.g., Lys amino or His imidazole) to achieve the same purpose but at much higher concentrations or valences. On the other hand, increasing the charge valence of substrate can effectively reduce the CCC and enhance probe sensitivity with a plateau reached at valence of 2 or 3 due to an intrinsic trade-off in the sensor working window (i.e., a set of peptide concentrations where the color pattern differs before/after proteolysis).[53]

Table 1.3. The critical coagulation concentration (CCC) of various ligated AuNPs with three segments. The aggregation induced by electrostatic fragment (EF), thiolate fragment (TF), and aromatic fragment (AF) is through electrostatic, covalent, and π-π stacking interaction, respectively.

[a] "N.D." indicates NP aggregation Not Detected under the tested conditions.

Ligand type	Sample	EF (μM)	TF (μM)	AF (μM)
Native	**Citrate-Au**	1	2	2
Polyphenols	**EGCG-Au**	20	N.D. [a]	N.D.
	TA-Au	20	50	N.D.
Phosphine ligands	**TCEP-Au**	0.5	5	N.D.
	DPPS-Au	5	50	100
	BSPP-Au	10	N.D.	N.D.
Thiolate ligands	**DTT-Au**	1	50	N.D.
	MPA-Au	5	50	50
	MPS-Au	10	50	N.D.
	GSH-Au	50	50	N.D.
	HS-PEG$_{\sim 110}$-COOH-Au	50	100	N.D.
	LA-PEG$_{12}$-COOH-Au	N.D.	50	N.D.
	LA-ZW-Au	50	50	N.D.
Macromolecular ligands	**X$_4$C$_4$-Au**	20	N.D.	N.D.
	PAA-Au	5	N.D.	N.D.
	PSS-Au	0.5	10	5
	PVP-Au	2	10	5
	LA-PIMA-PEG$_{15}$-Au	N.D.	N.D.	N.D.
	BSA-Au	N.D.	N.D.	N.D.

In the second aspect of electrostatic based aggregation, BSPP and DPPS ligands are structurally similar and are differentiated by their number of sulfonates (see structures in Figure 1.1b), where the measured zeta potential is -31.3 ± 1.8 mV and -25.2 ± 0.3 mV, respectively. Typically, highly charged nanoparticles have strong electrostatic repulsion, reduced van der Waals attraction, long Debye lengths, and thus good colloidal stability. That is, BSPP-AuNPs would be less sensitive than DPPS-AuNPs upon counterion titration, e.g., the CCC of DPPS-AuNPs and BSPP-AuNPs in the presence of NaCl is 50 mM and 100 mM, respectively; and the CCC of DPPS-AuNPs and BSPP-AuNPs in the presence of EF is 5 μM and 10 μM, respectively (Tables 1 and 3). Experimentally, BSPP-AuNPs were more resistant to charge-induced aggregation, thus giving rise to a wide working window for good sensor performance with less background interference, albeit with a minor compromised sensitivity (Figure S1.9a-b). To summarize, the choice of a peptide/AuNP pair as a good color sensor is determined by the charge valence of counterions and the matched colloidal stability, e.g., low charge valence shall be paired with weak stability or vice versa (Figure S1.9).

To better understand the interparticle interactions, reversibility experiments were carried out for the EF peptide/BSPP-AuNPs aggregates employing several solvents and surfactants (10 mM). In Figure 1.4a,b, the gold pellet (3.4 nM, 100 μL) freshly clustered by EF peptide (1.62 mM, 2.4 μL) readily disassociated and returned to red in the presence of sodium dodecyl sulfate (SDS). The excess anionic SDS scavenges the positively charged EF peptides, thus restoring the electrostatic double layer repulsions between particles.[23] In addition, shifting the pH to 11 also fully recovered the BSPP-AuNPs, which is likely due to (i) the deprotonation of the guanidinium ions and restauration of the electrostatic repulsion between nanoparticles, and/or (ii) high

concentration of OH^- that deprotonates the native citrate residues under basic conditions, thus leading to interparticle electrostatic repulsions.

The TF peptide contains a divalent-Cys and bridges AuNPs capped with citrate, TCEP, PVP, and PSS molecules. Here, the determined CCC values are at the same range compared to that of DTT-induced aggregation (Table 1.1 and 1.3). For instance, both TF peptide and DTT triggered instant color changes on citrate-AuNPs in the range of 2-5 μM or more (Figure 1.4c). This range is lower than a previous reported value because of the different fraction of thiolate segments in the solution (here, ~100% purity, Figure S1.6).[15] Notably, the TF peptide could not aggregate DPPS- or BSPP-AuNPs within 1 h despite Au-S being stronger than Au-P bonds, which agrees well with the data shown for DTT test above (Figure 1.3b). Thiolate ligand-capped AuNPs were insensitive to TF peptide titration. However, unlike DTT molecule the TF peptide did not show stabilizing effect for AuNPs at high concentrations. Of note, we have previously reported that the tetravalent-Cys peptide did not improve the sensor performance rather compromising the working window due to dangling and reactive sulfhydryl undermining the overall colloidal stability when appended with a stabilizing moiety.[15] In Figure 1.4d, the aggregation based on covalent coupling was also validated using the same reversibility experiments, where the gold pellet (3.4 nM, 100 μL, citrate-AuNPs) freshly clustered by TF peptide (980 μM, 1 μL) could not be redispersed in any of the surfactants/solvents employed.

The Phe-rich AF peptide aggregates AuNPs coated with citrate, PVP, and PSS molecules, and the CCC values are summarized in Table 1.3. In a previous work, we found that at the minimum, Phe-Phe was needed to induce π-π stacking while a single Phe only yielded hydrophobic interactions. In addition, the AF peptide without a Cys residue could not directly bridge aromatic ligands (e.g., DPPS and TA) via π-stacking, which is likely uncoupled by the

hydration layer initiated by the ligands.[25] That is, the AF peptide could also aggregate AuNPs capped with ligands that do not display any aromatic moiety (i.e., citrate, PVP, and PSS). In Figure 1.4f, the purple gold pellet (3.4 nM, 100 μL) clustered by AF peptide (6.2 mM, 10 μL) could be redispersed to red in organic solvents including dimethyl sulfoxide (DMSO) and dimethylformamide (DMF). This indicates prevalent π-π interactions in the AF peptide/AuNP pellet. As such, the design of AF eliminates the concerns of peptide functional loss in complex milieu due to oxidation and charge scavengers.

The redispersion of peptide/AuNP aggregates reveals the critical role of Arg/Cys/Phe residues, which govern the interplays among nanoparticles of a specific coating. Overall, the EF peptide crosslinks AuNPs capped with compact and charged ligands such as TA, DPPS, BSPP, or X4C4 molecules. Nonetheless, the EF peptide cannot associate NPs coated with charge-neutral ligands such as PVP, which could be clustered by the TF or AF peptide through covalent coupling or π-π stacking interactions. In addition, the TF and AF peptide require a direct contact of the Cys-sulfhydryl to the Au atom, and thus cannot aggregate well-passivated surfaces including thiolate and sulfonated phosphine ligand-AuNPs; while a few of these NPs strongly interact with the EF peptide due to the charged terminal groups.

Peptide optimization and protease detection

Previous reports also stressed the limitations of aggregation-based colorimetric sensors under dynamic condition, e.g., the electrostatic attraction-governed systems were largely impeded in complex biological media such as saliva and human plasma due to the abundance of negatively charged proteins forming a protein corona and/or scavenging the aggregating counterions. In addition, the electrostatic interactions between the Arg-guanidine and ligand carboxylate were sensitive to the environmental pH because of protonation/deprotonation

status.[23] Efforts were input to improve the sensor performance using Cys-/Phe-coded substrates, nonetheless, these peptides may suffer from oxidative and ionic conditions due to the requirement of reduced sulfhydryl and moderate surface passivation.[15, 25] Therefore, combining all these interparticle forces in one peptide substrate may expand the types of ligated AuNPs for use and retain the peptidic function under complex biological media.

The 'Mega' peptide (DDDTSAVLQ↓SG*FFRCR*P*C*, Table 1.2) was customized to encompass three functional domains composed of (i) an N-terminal stabilizing domain made of three Asp (DDD) for neutralizing the net charge of the substrate and minimizing interactions with NPs, (ii) a central Mpro cleavage site consisting of TSAVLQ↓SGF, and (iii) a C-terminal destabilizing domain for aggregating colloidal gold (Figure 1.1a). The destabilizing domain has two Arg and Phe for promoting electrostatic and π-π stacking interactions respectively, and two Cys for sequestering surface Au, thus promoting covalent interplay. Here, we hypothesize that proteolysis of the intact Mega peptide will lead to a strong aggregating segment and subsequently flocculate ligated AuNPs via a combination of interactions, thus producing intense color changes under various conditions.

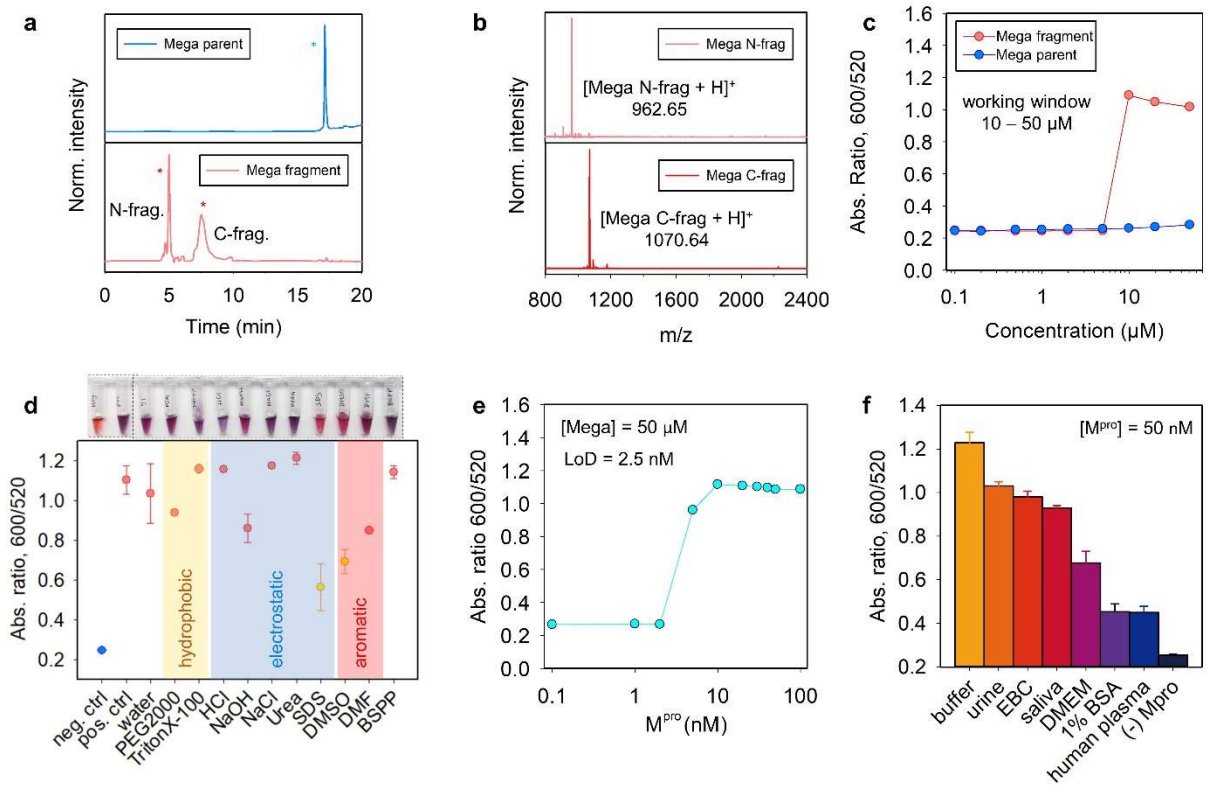

Figure 1.5. Improved performance of Mega peptide in colorimetric sensor. **(a,b)** HPLC and ESI-MS data confirm that M^{pro} cleaves the Mega peptide between Q and S. Peaks with * are the intact peptide (blue); the fragments are in red. **(c)** Ratiometric signal (Abs_{600}/Abs_{520} at 10 min readout time) recorded from BSPP-AuNPs (3.4 nM, 100 μL) incubated with various amount of intact Mega (red) and the fragments (blue). **(d)** White-light image (top) and quantified reversal color change (bottom) of the Mega/AuNP pellet in different surfactant solutions (10 mM, 100 μL) or solvents (100 μL). The redispersion in a SDS solution and DMSO solvent indicates dominant electrostatic and aromatic forces with scarce covalent bonding. **(e)** Ratiometric absorbance as a function of M^{pro} concentration. Conditions used the Mega substrate (100 μM), BSPP-AuNPs (3.4 nM), and a 10 min assay time. The determined limit of detection is 2.5 nM in Tris buffer. **(f)** Sensor performance in other biological media. Positive control used the buffer with M^{pro} (100 nM), and negative control used the buffer without M^{pro}. Error bar = standard deviation (n = 3).

Figure 1.5a shows the HPLC profiles of the synthetic Mega peptide before and after proteolysis by Mpro. Figure 1.5b indicates that the cleavage of Mega peptide liberated the SGFFRCRPC fragment (calcd. 1070.49; found, 1070.64). We first determined the working window for Mpro detection by recording the ratiometric absorbance (Abs_{600}/Abs_{520} at 10 min) after addition of AuNPs (3.4 nM, 100 μL) to the parent and its fragments of varying concentrations (i.e., 0 − 50 μM). We selected BSPP-AuNPs as a representative case for the sake

of improved colloidal stability and good sensing performance. As shown in Figure 1.5c, the intact Mega peptide caused no NP aggregation at the tested concentrations. In comparison, addition of the fragments exceeding 5.0 μM induced a noticeable color change in buffer and sizeable ratiometric absorbance signal. Thus, we defined 10-50 μM as the working window for the Mega peptide/BSPP-AuNPs pair. The working window of other combinations involving different surface coatings is provided in Figure S1.10, where the AuNPs capped with citrate, DPPS, BSPP, MPA, MPS, GSH, HS-PEG-COOH, LA-ZW, X_4C_4, and PSS showed good sensing values. The choices of AuNP type are enlarged for colorimetric sensors due to the strong aggregating propensity of the Mega segment that renders diverse interactions. Regardless of the various surface coatings, high concentrations of Mega peptide in the assay would benefit the probe sensitivity and thus 50 μM was defined as the optimal substrate concentration for the next experiments.

The limit of detection (LoD) was then investigated by incubating the Mega peptide (50 μM) with varying amounts of Mpro (0-100 nM) in Tris buffer (TB, 20 mM, pH 8.0) in a 20 μL assay volume for 3 h. Next, a dispersion of BSPP-AuNPs (3.4 nM, 100 μL) was added as the color agent. Figure 1.5c shows the ratiometric signal as a function of Mpro concentration. Therefore, the LoD for Mpro was 2.5 nM in Tris buffer; analysis used a previous reported method.[54] Of note, Mpro has no effects on the stability of BSPP-AuNPs. The exact levels of the Mpro that are clinically relevant in respiratory fluids of COVID-19 patients still remain uncertain,[58] but our detection limit is about 5- to 20-fold more sensitive than previous reported colorimetric or fluorescent probes, e.g., previous NP-based colorimetric assays from our group relying on covalent, π-π stacking and electrostatic interactions reported LoDs for Mpro about 10 nM, 16 nM, and 30 nM, respectively.[15, 23] Lin et al. also developed an peptide/AuNP system

based on electrostatic interactions and reported an LoD of 10 nM.[59] Another related work using a fluorogenic substrate reported an LoD of 50 nM.[60] Similarly, the commercial fluorogenic substrates (e.g., Covidyte™ EN450 substrate) typically detect Mpro as low as 20 nM. We attributed the improved detection limits to the strong aggregating propensity of the Mega segment, which contains Arg, Cys, and Phe, and thus, renders versatile interparticle interplays including electrostatic, covalent, and aromatic interactions. This results in substantially lower amounts of fragment needed for initializing color changes. To this end, Figure 1.5d shows that the Mega peptide/BSPP-AuNP aggregates can be partially redispersed into a SDS solution and DMSO solvent, indicating prevalent π-π stacking and electrostatic interactions with a scarce covalent bonding, presumably the good surface passivation of BSPP ligands impeding the formation of two Au-S bonds on two different particles in a short period.

Matrix effect

Next, we evaluated the matrix effects by first incubating the Mega peptide (50 μM) with Mpro spiked in 20 μL of different media for 3 h, such as TB (20 mM, pH 8.0), exhaled breath condensate (EBC), 1% bovine serum albumin (BSA) solution, human plasma, Dulbecco's Modified Eagle's Medium (DMEM), urine, and pooled human saliva. Subsequently, the BSPP-AuNP dispersion (3.4 nM, 100 μL) was added to reach a 100 nM protease concentration, and the ratiometric absorbance at 10 min was recorded (Figure 1.5f). The Mega peptide/BSPP-AuNP showed good performance not only in TB and EBC, but also in other complex media such as urine and pooled saliva. This is attributed to the complementary interparticle forces rendered by the Mega segments. This also indicates that enzymatic cleavage did occur in the matrixes and previous reports showing the quenched aggregations are most likely due to protein corona non-specifically binding either the NPs or the released peptide segments.[24, 61] For instance, EF

peptide/BSPP-AuNP is limited in use in pooled saliva due to charge scavengers binding to the working peptide segments;[23, 24] and the TF peptide/citrate-AuNPs showed no color change in human plasma presumably because the protein corona formation on the AuNPs.[15, 25] Control assays showed that the BSPP-AuNPs were in the tested matrixes except human plasma (i.e., about 40% aggregation level in human plasma only, Figure S1.11).[49]

Finally, we would like to note that (i) the present multifactorial design does not hold surface coverage constant, and (ii) the aggregation trend may not extrapolate to other NP compositions/morphologies.[3, 62] We emphasized that this study used a large excess of ligand during the ligand exchange and thus ensured maximum surface coverage.[63] (iii) The size of the NPs could also impact the results: Large AuNPs with the same coating might have weaker stability and thus lower CCC due to compromised entropy stabilization (from ligands) relative to van der Waals affinity (from NPs).[29, 38] Larger NPs also have a higher absorption cross-section and could produce intense color changes.[29] Thus, large NPs might lead to good sensitivity but a narrow working window or vice versa. (iv) We also could not exclude the possibility of a false positive result from off-site target of the Mega peptide by other enzymes (e.g., gingipains[64]) in the pooled saliva assays. (v) DMEM cell growth media, 1% BSA solution, and human plasma still impeded the aggregation kinetics of the Mega peptide/BSPP-AuNP by more than 50% presumably because of high level protein corona formation (Figure 1.5f).[49] A previous report indicates that BSA at 0.2 μM could build protein corona and thus stabilization effect on citrate-AuNPs.[15] A dilution factor of 5 and 20 is required for 1% BSA and plasma, respectively, to achieve successful aggregation of BSPP-AuNPs upon mixing with Mpro-incubated Mega peptide (Figure S1.12).

1.3 Conclusion

AuNPs coated with 19 ligands ranging from labile molecules to multicoordinating macromolecules were used as colorimetric agents, and their performance in aggregation-based colorimetric assays for protease detection were evaluated. The surface coatings favoring electrostatic, covalent, and π-π stacking interactions were optimized using three customized peptides. Our results showed that AuNPs coated with TA, DPPS, BSPP, or X4C4 ligands were the best for electrostatic-based aggregation. These ligands all have a low molecular weight, compact size, high charge valence, and a high degree of aromaticity. In addition, AuNPs coated with citrate or PVP were the best for dithiol-induced and π-π stacking interactions-based aggregation. These ligands generally have hard Lewis base anchoring groups and thus weak binding strength. We also provided the rationale for peptide-based interactions in terms of side chain type and number, e.g., the good performance of electrostatic-based sensors requires aggregating peptides of low charge valence to be paired with charged NPs of weak stability or vice versa. We then designed and tested a combination of the so-called Mega peptide and BSPP-AuNPs as an optimized colorimetric sensor where the aggregation is driven by both electrostatic and aromatic forces. By quantifying the color change with measurable ratiometric absorbance, we have determined the LoD was 2.5 nM for Mpro. This sensor not only performs well in buffer and EBC, but also in complex biological samples such as saliva and urine.

1.4 Acknowledgements

Chapter 1, in full, is a reprint of the material as it appears in American Chemical Society in Applied Materials & Interfaces 2023. Jin, Zhicheng; Yeung, Justin; Zhou, Jiajing; Retout, Maurice; Yim, Wonjun; Fatjová; Gosselin, Bryan; Jabin, Ivan; Bruylants, Gilles; Mattoussi,

Hedi; O'Donoghue, Anthony; Jokerst, Jesse. The thesis author was a primary investigator and author of this paper.

CHAPTER 2

An Approach to Zwitterionic Peptide Design for Colorimetric Detection of the Southampton Norovirus SV3CP Protease

Justin Yeung,[a] *Zhicheng Jin,*[b] *Chuxuan Ling,*[b] *Maurice Retout,*[b] *Elany Barbosa da Silva,*[c] *Manan Damani,*[c] *Yu-Ci Chang,*[d] *Wonjun Yim,*[d] *Anthony J. O'Donoghue,*[c] *Jesse V. Jokerst*[b,d,e]*

[a]Department of Bioengineering, University of California San Diego, La Jolla, CA 92093, United States

[b]Department of NanoEngineering, University of California, San Diego, La Jolla, CA 92093, United States

[c]Skaggs School of Pharmacy and Pharmaceutical Sciences, University of California, San Diego, La Jolla, CA 92093, United States

[d]Materials Science and Engineering Program, University of California, San Diego, La Jolla, CA 92093, United States

[e]Department of Radiology, University of California, San Diego, La Jolla, CA 92093, United States

Abstract

Noroviruses are highly contagious and are one of the leading causes of acute gastroenteritis worldwide. Due to a lack of effective antiviral therapies, there is a need to diagnose and surveil norovirus infections to implement quarantine protocols and prevent large outbreaks. Currently, the gold standard of diagnosis uses reverse transcription polymerase chain reaction (RT-PCR), but PCR can have limited availability. Here, we propose a combination of a tunable peptide substrate and gold nanoparticles (AuNPs) to colorimetrically detect the Southampton norovirus 3C-like protease (SV3CP), a key protease in viral replication. Careful design of the substrate employs a zwitterionic peptide with opposite charged moieties on the C- and N- termini to induce a rapid color change visible to the naked eye; thus, this color change is indicative of SV3CP activity. This work expands on existing zwitterionic peptide strategies for protease detection by systematically evaluating the effects of lysine and arginine on nanoparticle charge screening. We also determine a limit of detection for SV3CP of 28.0 nM with comparable results in external breath condensate, urine, and fecal matter for 100 nM of SV3CP. The key advantage of this system is its simplicity and accessibility, thus making it an attractive tool for qualitative point-of-care diagnostics.

2.1 Introduction

Human noroviruses (HNV) are one of the leading causes of gastrointestinal illness and are responsible for an estimated 685 million cases worldwide per year according to the Centers for Disease Control and Prevention.[65] In the United States alone, HNV is the leading cause of outbreaks from contaminated food, accounting for about 50% of food-related illness outbreaks.[66] These outbreaks are common in settings such as schools, military barracks, cruise ships, and resorts. Importantly, HNV can be transmitted from person-to-person and through surfaces contaminated by viral particles from emesis, stool, and aerosolized particles, unlike food poisoning from toxins (e.g., those produced by the bacteria Staphylococcus aureus).[66, 67] Due to the lack of vaccines or anti-viral therapies, outbreak management is reliant on diagnostic evaluation followed by quarantine. The most common diagnostic methods are enzyme immunoassays and reverse transcription polymerase chain reaction (RT-PCR).[68, 69] However, these methods are rarely available at the point of care.

Ideally, the goal is to have quick isolation and identification of infected people to prevent additional spread, which can be achieved with point of care testing. Colorimetric sensors utilizing gold nanoparticles (AuNPs) can be a cost-effective and intuitive diagnostic platform that can resolve the inherent limitations of established protocols. AuNP-based diagnostics have gathered attention regarding their use in in vitro diagnostics due to their distinct physical and optical properties including localized surface plasmon resonance (LSPR) and fluorescence resonance energy transfer (FRET).[9] Aggregation of these particles can induce interparticle plasmon coupling and exploit the AuNPs' ultrahigh extinction coefficient to generate a significant absorption band shift in the visible region of the electromagnetic spectrum, thus resulting in a pronounced red-to-blue color change visible to the naked eye.[9] Additionally,

surface modifications of AuNPs can provide diverse functionalization options that allow for robust interfacing of the particles through electrostatic, dithiol bridging, or amphiphilic interactions to promote aggregation.[15, 23, 25, 70]

To bridge the gap between these interparticle interactions and viral particle screening, peptides can be used as an effective probe for proteolytic detection due to their diverse and tunable functional groups found on amino acid side chains. By exploiting the critical proteolytic post-processing step within the viral protein lifecycle, custom peptide substrates can be engineered to be activated in the presence of viral proteases to disrupt the plasmonic coupling of AuNPs and subsequently produce a pronounced color change indicative of proteolysis.[71] More specifically, the proteolytic peptide products can be tuned to aggregate the AuNPs stabilized by their repulsive electrostatic double layer via charge screening.[20, 23] Similar approaches using AuNPs to electrostatically detect heavy metal ions in colorimetric assays have also been reported.[72] Plasmonic sensing has also been used in detecting other proteases including thrombin, furin, trypsin, and SARS CoV-2 Mpro.[6, 16, 23, 73] In principle, this approach can be generalized to other proteases by simply adjusting the cleavage recognition sequence to be suitable for molecular recognition between the target enzyme and substrate.

Here, we build on prior work for zwitterionic peptides, $(Asp)_n$-$(AA)_x$-$(Arg)_m$, which are known to induce AuNP aggregation following proteolysis by examining the effects of lysine residues in conjunction with arginine residues on AuNP charge screening (e.g., $(Asp)_n(Glu)_o$-$(AA)_x$-$(Arg)_m(Lys)_p$).[9] The kinetics of the AuNPs with peptides were studied, and the aggregation state was measured. We then evaluated the generalizability of this approach by applying this system to colorimetrically measure the Southampton norovirus 3C-like protease (SV3CP). SV3CP plays a key role in the processing of a 200 kDa polyprotein encoded by ORF1,

which is essential to viral replication, and lacks human homologues, making it an ideal target for diagnosis.[74] The specificity of our designed substrate was examined, and the protease detection limit was determined to be 28.0 nM. Finally, the plasmonic sensing system's performance was tested in relevant biological matrices and had a notable performance in external breath condensate, urine, and 1% fecal matter. This approach can be a valuable and economical tool for HNV diagnosis.

2.2 Results and Discussion

Rationale

Here, we use bis(p-sulfonatophenyl)phenylphosphine modified AuNPs (BSPP-AuNPs) to interface with the cleavable zwitterionic peptide substrates. To obtain these particles, a ligand exchange was performed according to our previous studies, starting with citrate-AuNPs to BSPP-AuNPs.[29, 39] Functionalization of AuNPs with the BSPP ligand provided the nanoparticles with considerable colloidal stability relative to the native citrate particles.[15] This stability is due to the strong negative charges found in the sulfonate groups of BSPP, effective gold-phosphorous gold coordination, steric hindrance from bulky aromatic rings, and strong electrostatic double layer repulsions.[75] As a result, the BSPP-capped nanoparticles can remain colloidally stable in various media, making them suitable for use in buffers and higher salt concentrations.

Figure 2.1a shows that the zwitterionic peptide mimics these salts (e.g., NaCl) because it carries oppositely charged termini (e.g., $(Asp)_n$ and $(Glu)_o$ vs. $(Arg)_m$ and $(Lys)_p$) flanking the SV3CP-specific cleavage site $(AA)_x$. With $n + o \geq m + p$ (e.g., $(Asp)_n(Glu)_o$-$(AA)_x$-$(Arg)_m(Lys)_p$), the peptide substrate carries a net neutral or negative charge, minimizing its interactions with the BSPP-AuNPs due to the negatively charged sulfonate groups carried by the ligand. Upon proteolysis, the peptide is segmented into its corresponding negatively charged and

positively charged fragments, thereby altering the electrophoretic properties of the substrate. The resulting positive cleavage product can then trigger the collapse of the nanoparticle suspension via electrostatic interactions, thus creating a color change visible to the naked eye.

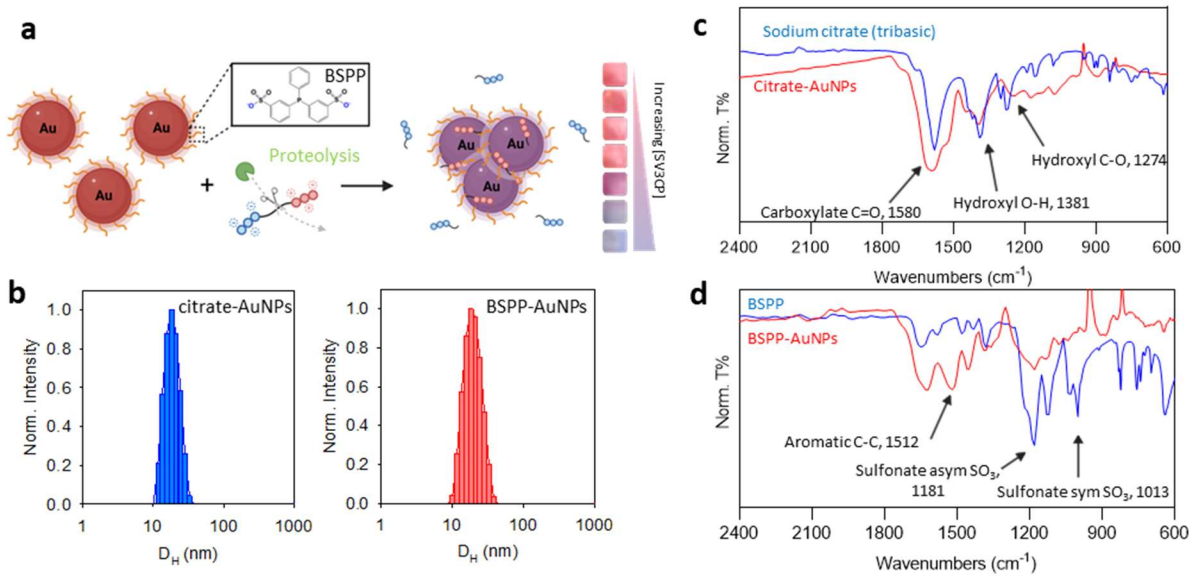

Figure 2.1. Mechanism of the plasmonic sensing system and characterization of the citrate-AuNP to BSPP-AuNP ligand exchange. **(a)** Schematic illustration of plasmonic sensing using BSPP-AuNPs. The green cartoon represents SV3CP; red and blue circles represent the positively and negatively charged amino acids, respectively, flanking the cleavage site. **(b)** DLS profiles of citrate-AuNPs (blue) and BSPP-AuNPs (red). FTIR spectra over the range of 2400-600 cm-1 of **(c)** citrate-AuNPs and **(d)** BSPP-AuNPs. The C=O signatures are associated with the carboxylate groups in sodium citrate, while the aromatic C-C and S-O signatures are from BSPP. This is indicative of a successful ligand exchange to make the BSPP-AuNPs.

Characterization of nanoparticle ligand exchange

To validate the successful ligand exchange of the native citrate particles with the BSPP ligand, we characterized the BSPP-capped particles using dynamic light scattering (DLS) and zeta potential measurements (Table 2.1, Figure 2.1b). The hydrodynamic diameter (DH) and polydispersity index (PDI) show slight increases with a slight decrease of the zeta potential, characteristic of the stronger negatively charged sulfonate groups relative to the native citrate

anions. These results are largely consistent with our past studies of this specific ligand exchange.[23, 70] Furthermore, a Fourier transform infrared (FTIR) spectroscopy of the particles before and after the ligand exchange shows the removal of most of the native citrate and binding of the BSPP ligand onto the nanoparticle surface (Figure 2.1c, 2.1d), as noted by symmetrical and asymmetrical stretching of the S-O bond from the BSPP ligand, indicating a successful ligand exchange.

Table 2.1. Hydrodynamic size and zeta potential of citrate-AuNPs and BSPP-AuNPs.

Sample	**DLS: D_H (nm)**	**DLS: PDI**	**Zeta: ζ (mV)**
Citrate-AuNPs	18.9	0.22	-29.8 ± 2.4
BSPP-AuNPs	19.9	0.23	-31.0 ± 1.4

Interactions between the nanoparticles and SV3CP-cleavable peptides

As mentioned, the zwitterionic peptide design describes a net neutral charge of the intact peptide by balancing repeating units of aspartic acid (Asp, D) and arginine (Arg, R).[23] The simplicity of this design lies in solely altering the cleavage recognition site flanked by the charged amino acids when targeting new proteases. More specifically, the flanking sites consist of an N-terminal charge-shielding site made of repeating Asp units and a C-terminal aggregating site made of repeating Arg units. However, in the case of SV3CP, literature has identified a SV3CP-cleavage recognition sequence of EFQLQ↓GK, notably containing glutamic acid (Glu, E) and lysine (Lys, K).[68] Glu and Asp are structurally very similar, with Glu containing one additional methylene group in its side chain; both carry a charge of -1 at a pH of 8. The issue lies in the difference in aggregation propensity due to presence of the Lys residue, as it remains in the C-terminal region of the cleavage site and will subsequently be liberated in the positively

charged aggregating site. Arg is often the preferred amino acid over Lys for giving cationic properties to peptides, as its positive charge is stabilized by several resonance forms of the guanidine side chain, giving it a pKa of 12.0 in water versus Lys, which has a pKa of 10.4.[76-79] Additionally, the guanidium group can facilitate interactions in three possible directions, with anionic counterparts through its three asymmetrical nitrogen atoms.[70] Previously, the positively charged fragment was optimized to include two Arg residues for charge screening BSPP-AuNPs.[23] The difference in cationic properties between Lys and Arg suggests potential differences in their ability to charge screen the nanoparticles, which will be explored later. Here, we propose an initial peptide substrate N6: DADEFQLQ↓GKAR (net charge=0). Proteolysis by SV3CP of N6 results in the formation of two fragments: DADEFQLQ (net charge=-3) and GKAR (net charge=+2).

AuNP aggregates induced by the N6 peptide were first characterized using transmission electron microscopy (TEM) (Figure 2.2a, 2.2b). In the presence of intact N6 peptide, the BSPP-AuNPs remain colloidally stable, with the nanoparticles clearly aggregating upon incubation with N6 fragments. DLS profiles of the particles incubated with intact and SV3CP-cleaved N6 peptide further support this, as shown by the nearly 50-fold increase in hydrodynamic size (D_H) indicative of large aggregates (Figure 2.2c). To quantitatively assess the aggregation state and resulting color change of the nanoparticles, the UV/Vis spectra of the nanoparticles was analyzed (Figure 2.2d). Incubation with the N6 fragment led up to a two-fold decrease in the LSPR at 520 nm, with a seven-fold increase in absorbance in the 600-650 nm region. We then defined the ratiometric signal, Abs_{600}/Abs_{520}, as a metric to quantify aggregation intensity and color change.[15, 23, 25, 70]

Next, we investigated the aggregation kinetics of the nanoparticles when incubated with increasing concentrations of N6 fragments (Figure 2.2e). Here, we see that aggregation is both time- and concentration-dependent. The 10-minute readout of the ratiometric signal shows clear differences across varying concentrations of N6 fragment and provides enough time for the nanoparticles to reach a notable aggregation state. As such, the 10-minute mark is used as the standard for reporting the ratiometric signal in future assays. High performance liquid chromatography (HPLC) and matrix-assisted laser desorption ionization–time-of-flight mass spectrometry (MALDI-TOF MS) (Figure 2.2f, 2.2g) also confirm the cleavability of N6 and precision of the SV3CP cleavage by detection of the N6 N-terminal fragment.

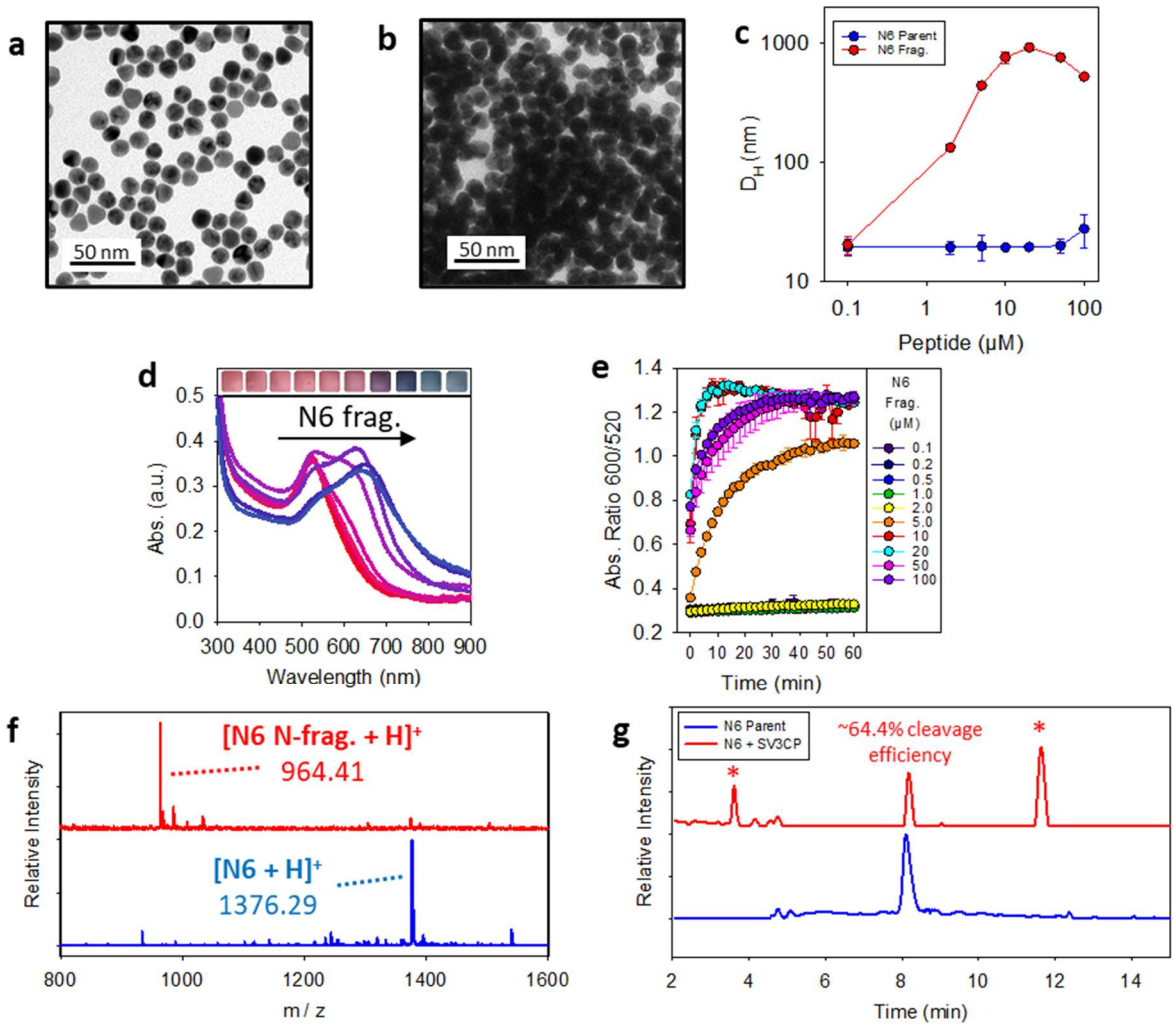

Figure 2.2. Characterization of AuNP aggregates with N6 fragments pre-cleaved by SV3CP. TEM images of the BSPP-AuNPs when incubated with **(a)** intact N6 and **(b)** SV3CP-cleaved N6 fragments. **(c)** DLS profiles of BSPP-AuNPs incubated with increasing concentrations of intact (blue) and SV3CP-cleaved (red) N6 peptide. No change was seen in the hydrodynamic diameter (DH) in the particles with the intact peptide whereas a sizable change is seen when incubated with N6 fragments of at least ~2 μM. **(d)** Optical absorption and color visuals of BSPP-AuNPs (3.4 nM, 100 μL) with increasing concentrations of N6 fragments. The arrow denotes the absorption band shift and corresponding color evolution. **(e)** Kinetic measurements of the ratiometric signal, Abs600/Abs520, were taken over 60 minutes for increasing concentrations of N6 fragments (e.g., 0.1, 0.2, 0.5, 1, 2, 5, 10, 20, 50, and 100 μM). The 10-minute readout showed a notable change in the ratiometric signal, which plateaus after 60 minutes. Error bars = standard deviation (n=3). **(f)** HPLC of N6 before and after incubation with SV3CP. '*' denotes the presence of new peaks due to proteolysis. N6 was incubated with SV3CP at a [E]:[S] ratio of 1:200 for 48 hours, resulting in a 64.4% cleavage efficiency. **(g)** MALDI-TOF mass spectrometry of N6 peptide before (blue) and after (red) incubation with SV3CP. Proteolysis is confirmed through the detection of the N6 N-fragment. Analysis of the cleavage was conducted on the crude proteolysis reaction; mass spectrometry of individual HPLC peaks was not suitable because the fractions had low yields.

Zwitterionic peptide dynamic range optimization

The dynamic range of various peptide derivatives of N6 was examined to determine the optimal sequence for plasmonic sensing of SV3CP (Figure 2.3). Table 2 details the sequences of the six peptides examined, along with their rationale. Computational folding data of each peptide is included in Figure S2.1. The dynamic range of each peptide is extracted by recording the ratiometric signal (Abs_{600}/Abs_{520}) at 10 minutes after addition of the BSPP-AuNPs (3.4 nM, 100 μL) to each peptide or pre-digested fragment at varying concentrations (e.g., 0.1 -100 μM). The lower limit of the dynamic range is determined by the critical coagulation concentration (CCC), the minimum concentration of peptide needed to induce coagulation of the AuNPs, of the pre-digested peptide while the upper limit is determined by the CCC of the intact peptide according to Equation S2.1. MALDI-TOF MS and HPLC confirmed the cleavability, or lack thereof, of each peptide (Figure S2.2).

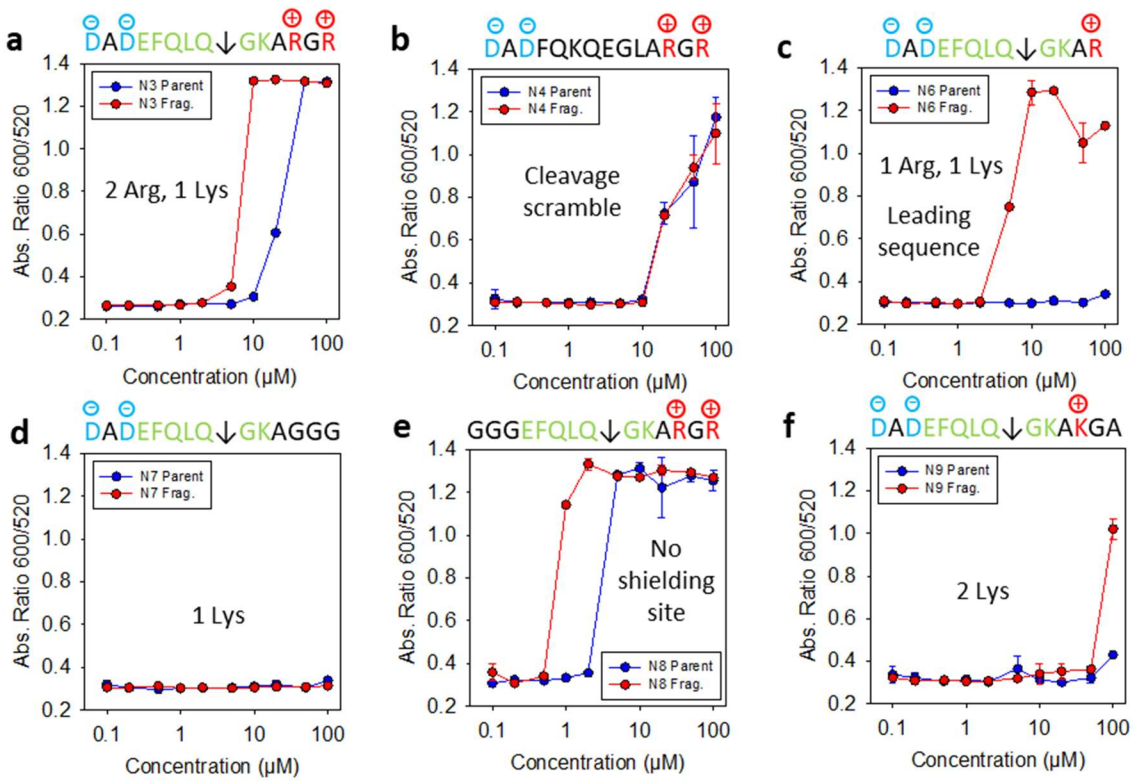

Figure 2.3. Dynamic range of peptides. Ratiometric signal (Abs_{600}/Abs_{520} at 10 min.) was recorded from BSPP-AuNPs when incubated with various amounts of **(a)** N3, **(b)** N4, **(c)** N6, **(d)** N7, **(e)** N8, and **(f)** N9 intact (blue) and SV3CP-cleaved (red) peptides. Amino acids units labeled in blue, green, and red correspond with charge-shielding, cleavage recognition, and aggregation respectively. Increasing additions of Lys and/or Arg result in lower detection limits in both the intact and fragmented peptides. This broadly follows the trends outlined in a peptide valence study based on the Schulz-Hardy rule.[53] Error bars = standard deviation (n=3).

Table 2.2. Peptide information (e.g., $(Asp)_n(Glu)_o$-$(AA)_x$-$(Arg)_m(Lys)_p$) and operating windows.

Peptide Name	Sequence	M. W. (g mol^{-1})	Net Charge [a]	Dynamic Range (μM) [b]	Rationale
N3	DADEFQLQ↓GKARGR	1588.8	0	2.9 – 7.2	single lysine, double arginine
N4	DADFQKQEGLARGR	1588.8	0	-	cleavage scramble
N6	DADEFQLQ↓GKAR	1375.7	-1	2.0 – 100.0	single lysine, single arginine; leading sequence
N7	DADEFQLQ↓GKAGGG	1390.6	-2	-	single lysine; minimized aggregating site
N8	GGGEFQLQ↓GKARGR	1458.8	+2	0.3 – 1.9	no shielding site
N9	DADEFQLQ↓GKAKGA	1475.7	-1	49.8 – 100.0	double lysine

[a] The electrophoretic property at pH 8.0; note that all peptides contain a free N-terminus (e.g., -NH−2 uncharged at pH 8.0) and an amidated C-terminus (e.g., -Am). **[b]** The dynamic range of each peptide was determined in Tris-buffer (TB) containing 150 mM NaCl and 5 mM DTT at pH 8.0.

In Figure 2.3a, N3, a zwitterionic peptide containing two arginine units in addition to the lysine inherently found in the cleavage recognition site, induced a notable color change. Pre-digestion of N3 with SV3CP results in a slightly lower CCC due to the liberation of the charge-shielding site and +3 charged fragment, however, the overall dynamic range of the peptide is narrow: 2.9 – 7.2 μM. A peptide with a scramble of the cleavage sequence in N3, named N4, confirmed that cleavage of the substrate is required to segment the peptide into its charged fragments and induce a notable difference in plasmonic coupling, as noted by the over six-fold increase in the ratiometric signal, between the intact and fragmented peptide (Figure 2.3b). Hence, N4 does not have a notable dynamic range, with both intact and SV3CP-incubated peptides having a similar effect as intact N3. Instead, the optimal sequence contains an aggregating site with a +2 charge when enzymatically cleaved. Specifically, our sequence, N6 (Figure 2.3c) varies the positively charged residues containing one lysine and one arginine versus two arginine units. Variations in the amount of lysine units were also examined (Figure 2.3d,

2.3f), but were unable to aggregate the AuNPs or required high concentrations of fragmented peptide in the case of N7 (one lysine unit) and N9 (two lysine units) respectively. Additionally, the charge-shielding site is needed to establish a larger dynamic range, as omitting this sequence can result in a nearly three-fold reduction in the dynamic range as shown by N8 (Figure 2.3e). Pre-digested N6 has a similar CCC as pre-digested N3, though the key difference lies in the CCC of the intact peptide, with the AuNPs retaining their colloidal stability in N6 concentrations of up to 100 μM. The resulting dynamic range has comparable sensitivity of the pre-digested peptide to our previously reported sequence but has a notably wider dynamic range.[23]

Our peptide design strategy shares some aspects discussed in prior work which used arginine, though lysine was not as thoroughly explored.[23, 24, 53] Increasing the amount of positively charged amino acids, arginine and/or lysine, results in the increasing charge valence of the liberated aggregating site and subsequent decrease in CCC, following similar trends summarized by the Schulz-Hardy rule.[53] Here, we report that additions of lysine units can result in more subtle changes of the CCC of AuNPs than arginine, as described by the behavior of N7 versus N6 or N9 (e.g., N6's CCC is 2.0 μM whereas N9's CCC is 49.8 μM). This can be attributed to the difference in pH-dependent charge stability of the functional groups found in arginine and lysine, where the resonance-stabilized guanidine group in arginine makes it a strong baser than lysine's simple ammonium ion.[76, 78, 79] The resulting modulation of the CCC through a combination of arginine and lysine can fine tune the electrostatic peptide-induced AuNP aggregation, hence, there is a nearly two-fold increase in dynamic range of N6 over its arginine counterpart.[23]

SV3CP detection and mechanistic study

We then used the optimal combination of N6 and BSPP-AuNPs to study our system's ability to detect SV3CP. Using a spectrophotometer, the limit of detection (LoD) for SV3CP was determined by Equation S2.1 to assess its clinical value. Based on the dynamic range of N6, a substrate concentration of 50 μM was used for all protein characterization studies. A minimum concentration of 2.0 μM of N6 is needed to aggregate the AuNPs, while the 50 μM of intact N6 should only slightly affect the colloidal stability of the particles. The enzyme assay was performed by incubating different concentrations of protease in TB-buffer with 50 μM of N6 in a 20 μL volume for 48 hours at 37°C followed by subsequent addition of 100 μL AuNPs for a colorimetric readout. The clinically relevant concentration of SV3CP remains unclear, but our system achieves nanomolar sensitivity with a LoD of 28.0 nM (Figure 2.4a). A shorter incubation time of 8 hours was also examined (Figure S2.3a), though it has a worse sensitivity with a LoD of 91.0 nM. This is an improvement over a previously reported FRET-based probe that showed a notable increase in signal starting at 250 nM.[80] As such, the standard incubation conditions for the subsequent assays reported uses 100 nM of SV3CP with a substrate incubation time of 48 hours at 37 °C. To further characterize the enzyme-substrate behavior of the custom substrate, a synthetic fluorogenic substrate, consisting of a similar peptide sequence conjugated to the 7-amino-4-methylcoumarin (AMC) fluorophore (*Ac*-EFQLQ-*AMC*) was used to determine the specificity constant (k_{cat}/K_m). For our substrate, a specificity constant of 739 $M^{-1}s^{-1}$ was observed (Figure 2.4b), which is in good agreement with sequences reported in prior works developed for genogroup-1 (Southampton like) proteases.[80, 81]

To test the specificity of our substrate to SV3CP, we cross-tested the effects of several related mammalian proteins on our sensing system including trypsin (e.g., cleaves at the C-

terminus of Arg or Lys), hemoglobin, salivary α-amylase (e.g. digests α-1,4-glucosidic bonds in starch)[82], thrombin (e.g., cleaves the Arg-Gly bond in fibrinogen), and bovine serum albumin (BSA). Figure 2.4c shows that only the positive control (e.g., 100 nM SV3CP), yields a notable optical signal and subsequent colorimetric readout. While our substrate can be non-specifically cleaved by trypsin (DADEFQLQGK↓AR), the resulting +1 charged fragment (AR) is not sufficient to disrupt the plasmonic coupling of the AuNPs, which agrees with our previous report.[53] Figure 2.4d gives additional insights into the enzyme-dependent activation of the colorimetric system. As a control, we heat-inactivated the protease by subjecting the SV3CP to high temperature conditions (60°C, 3 hours) prior to substrate incubation.[83] This is also intended to mimic the thermoregulatory immune response following infection. As expected, heat treating SV3CP results in the denaturation and inactivation of the protease, suggesting a correlation between colloidal activity and the course of the infection.

Having established the system's dependency on the substrate-enzyme interaction, we then investigated the mechanism by which the charged peptide interacts with the BSPP-AuNPs to ensure that aggregation of the particles is indeed electrostatically induced. Reversibility experiments were conducted by employing several solvents and surfactants (10mM) to better understand the interparticle interactions between N8/BSPP-AuNPs aggregates. In Figure 2.4e, the gold pellet (3.4 nM, 100 μL), freshly clustered by N8 peptide (1.55 mM, 1 μL), readily dissociated and returned to a pinkish state in the presence of sodium dodecyl sulfate (SDS). Here, the excess anionic SDS scavenges the positively charged peptides and restores the electrostatic double layer repulsions between the particles.[42, 84] NaOH also slightly redisperses the particles and can likely be attributed to the deprotonation of guanidium and ammonium ions at pH 11.0, restoring the electrostatic repulsions between nanoparticles.[23, 70]

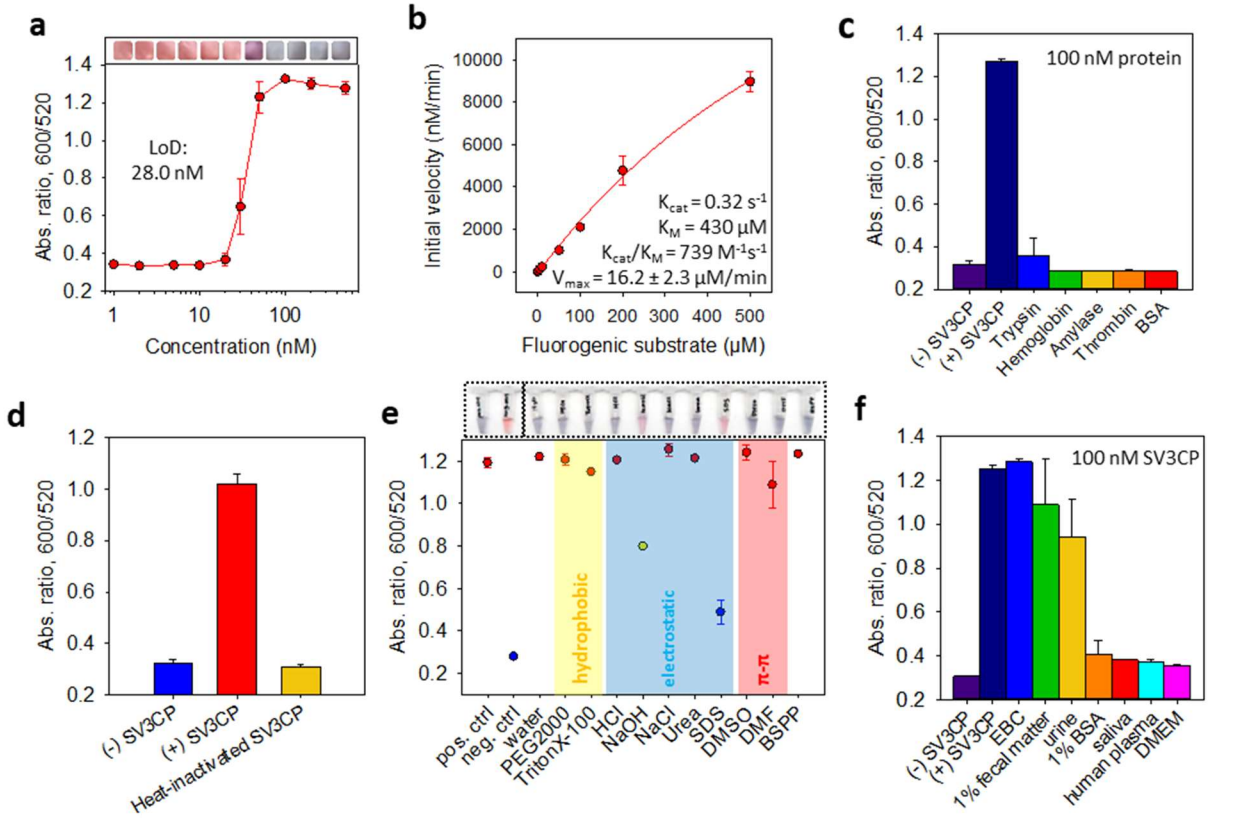

Figure 2.4. Sensitivity and specificity testing and sensing mechanism exploration. **(a)** Ratiometric absorbance as a function of SV3CP concentration with color visuals on top. N6 substrate and BSPP-AuNPs (3.4 nM) were employed. The substrate was incubated with the protease in TB buffer for 48 hours before addition of BSPP-AuNPs. **(b)** k_{cat}/K_m determination of the hydrolysis of fluorogenic substrate (*Ac*-EFQLQ-*AMC*) by SV3CP in 0.02M TB buffer, NaCl 150 mM, 5 mM DTT, pH 8.0. SV3CP (850 nM) was incubated with varying fluorogenic substrate concentrations (e.g., 0.1-500 µM). Data was fitted to the Michaelis-Menten equation (Equation S2.3). **(c)** Specificity testing of other mammalian proteins (100 nM) in TB buffer, including trypsin, hemoglobin, amylase, thrombin, and BSA. Samples with and without SV3CP served as positive and negative controls, respectively. **(d)** Thermoregulated heat inactivation of SV3CP (100 nM). SV3CP was heated at 60°C for 3 hours prior to substrate incubation for 48 hours. The resulting colorimetric readout shows the system's dependence on SV3CP-activity. **(e)** White-light image (top) and quantified reversal of color change (bottom). Redispersion in SDS indicates dominant electrostatic forces. **(f)** System performance in biological matrices. The positive control used 100 nM of SV3CP in buffer, and the negative control is buffer without SV3CP. Error bars = standard deviation (n =3).

Lastly, we examine the performance of our system in various biological matrices relevant to HNV pathology and detection. Viral particles are primarily transmitted through aerosolized particles during vomiting and fecal matter contamination during diarrhea. Thus, release of

SV3CP should theoretically occur in oral matrices such as saliva and exhaled breath and in stool samples for HNV-infected patients.[69, 85, 86] The colorimetric readout was determined in external breath condensate (EBC), 1% fecal matter, urine, 1% BSA, saliva, human plasma, and Dulbecco's modified Eagle's medium (DMEM) (Figure 4f). BSPP-AuNPs were stable in all biological matrices except fecal matter, which required a minimum 1 in 5 dilution to avoid matrix-induced aggregation of the AuNPs (Figure S2.3b). The performance of our system in increasing dilutions of fecal matter is shown in Figure S2.3c, which may be more clinically relevant to patient-derived samples due to the high-water content of diarrhea.[87] A 1 in 100 dilution is required to attain a notable colorimetric readout in fecal matter. This is likely attributed to the presence of complex polysaccharides found in fecal matter that can non-specifically inhibit proteins—this is a known issue for RT-PCR based assays.[88] When spiked with SV3CP in the presence of the N6 peptide, AuNPs aggregated in EBC, 1% fecal matter, and urine. Additionally, more complex media such as BSA, saliva, human plasma, and cell culture medium largely impedes the aggregation of the nanoparticles, likely due to the abundance of negatively charged proteins forming a protein corona around the nanoparticles and/or scavenging the aggregating counterions.[70, 89] Increasing dilution factors of these matrices, however, minimizes the aggregation impedance, as shown in a previous study.[9]

Overall, this approach offers a simple and intuitive alternative to conventional immunoassays that boasts label-free conditions without the need for complex laboratory equipment. Our previous studies have adapted similar systems to diagnostic kits for face coverings and dipstick testing.[23, 53, 82] With remarkable specificity to SV3CP and functionality in select HNV-related biomatrices, this system can be used to non-invasively monitor HNV

infections in the presence of >28.0 nM SV3CP (Figure 2.4a) to complement existing detection portfolios.[90]

2.3 Conclusion

An updated formula for zwitterionic peptides, $(Asp)_n(Glu)_o$-$(AA)_x$-$(Arg)_m(Lys)_p$, is reported to modulate the dispersity of BSPP-capped AuNPs and is applied to colorimetrically detect SV3CP, a key-protease implicated in the HNV viral lifecycle. We construct a label-free peptide (N6) in accordance with this formula, carrying a net -1 charge incapable of aggregating the negatively charged BSPP-AuNPs. Enzymatic cleavage of the peptide results in the liberation of a positively charged fragment, disrupting the plasmonic coupling between nanoparticles through electrostatic interactions. We quantified the color change using absorbance spectroscopy and showed the difference in aggregating propensity between arginine and lysine, providing optimizations of zwitterionic peptide design for colorimetric sensing. We then found the LoD of SV3CP in TB buffer to be 28.0 nM, with notable performance in EBC, 1% fecal matter, and urine using 100 nM of SV3CP. Cross-testing against other related mammalian proteins reveals no non-specific activation of the probe. Heat-denaturation of SV3CP confirms the critical role of enzymatic cleavage in mediating color change. The use of zwitterionic peptide/AuNP-based sensors does not require bioconjugation or sophisticated equipment, offering a promising solution for point-of-care qualitative diagnostics.

2.4 Acknowledgements

Chapter 2, in full, has been submitted for publication as it may appear in Royal Society of Chemistry in Chemical Communications 2023. Yeung, Justin; Jin, Zhicheng; Ling, Chuxuan; Retout, Maurice; Barbosa da Silva, Elany; Damani, Manan; Chang, Yu-Ci; Yim, Wonjun; O'Donoghue, Anthony; Jokerst, Jesse. The thesis author was the primary investigator and author of this paper.

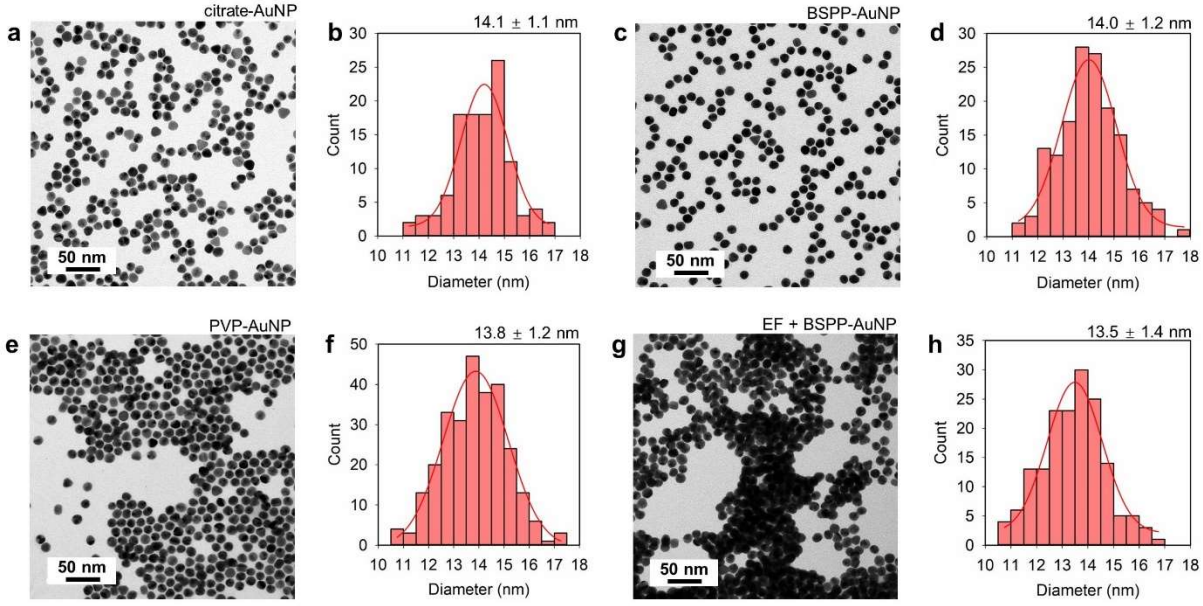

Figure S1.1. TEM images of the representative AuNPs. **(a)** The as-prepared citrate-AuNPs and **(b)** a histogram of particle size with an average diameter of 14.1 ± 1.1 nm. **(c)** The BSPP-AuNPs with **(d)** a diameter of 14.0 ± 1.2 nm. **(e)** The PVP-AuNPs with **(f)** a diameter of 13.8 ± 1.2 nm. **(g)** The BSPP-AuNPs incubated with 50 μM EF peptide with **(h)** a diameter of 13.5 ± 1.4 nm. Data were analyzed in ImageJ by counting more than 100 particles using a manual size method.

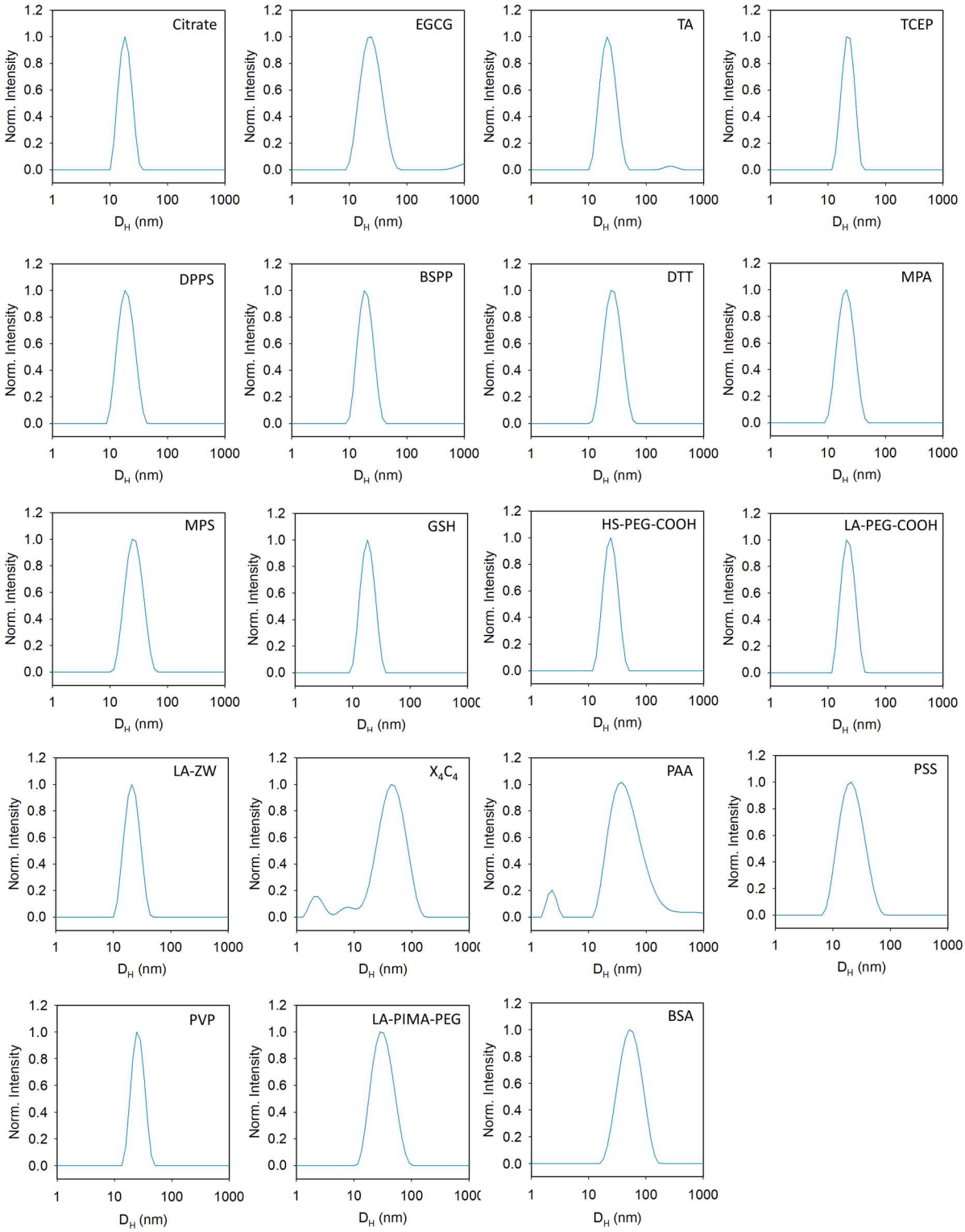

Figure S1.2. Hydrodynamic diameter (D_H) distributions obtained from dynamic light scattering of ligated AuNPs. The values and polydispersity index (PDI) are listed in Table 1.1.

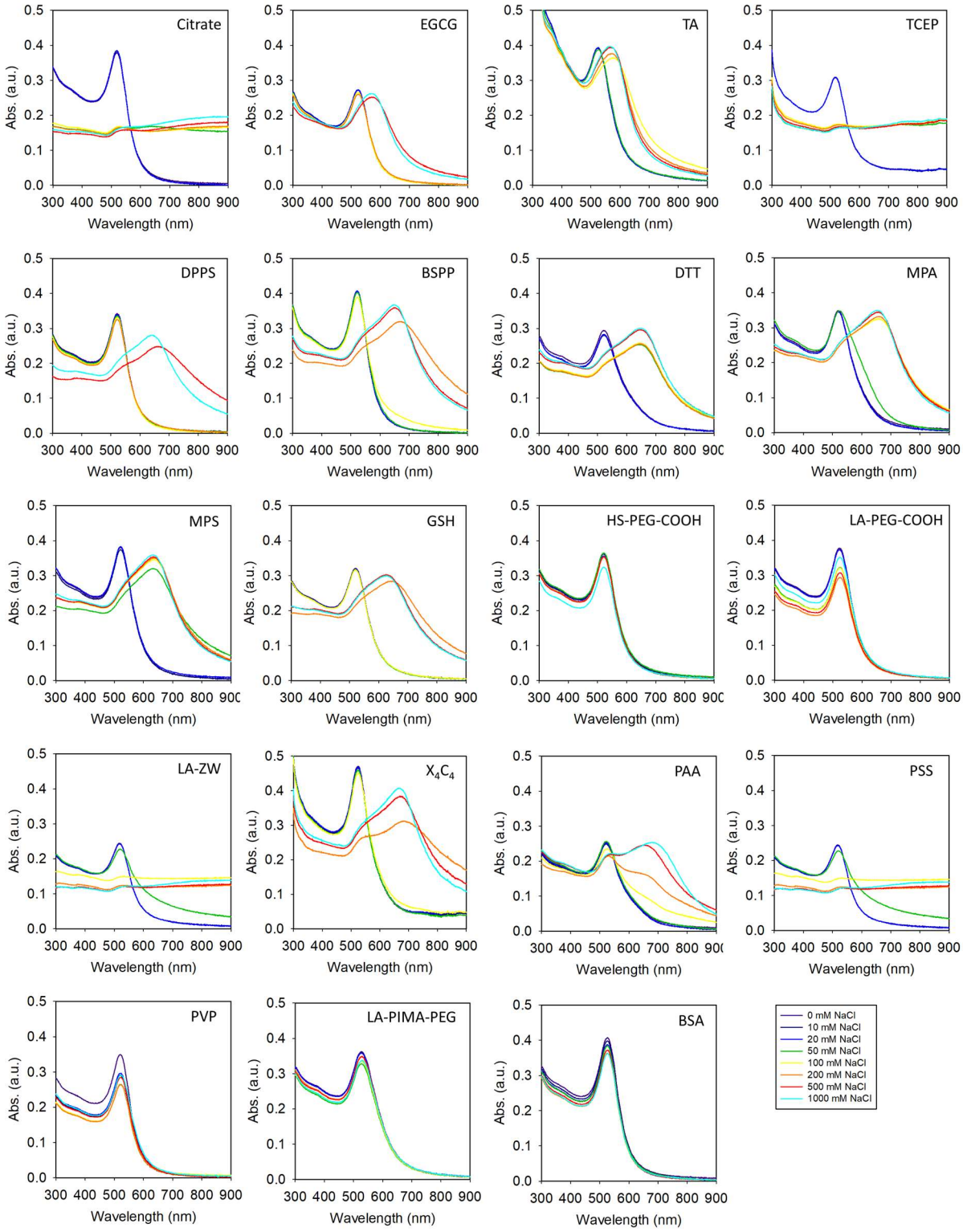

Figure S1.3. Absorption spectra of AuNPs capped with different ligands when incubated with various concentrations (0, 10, 20, 50, 100, 200, 500, and 1000 mM) of NaCl solution for 10 minutes.

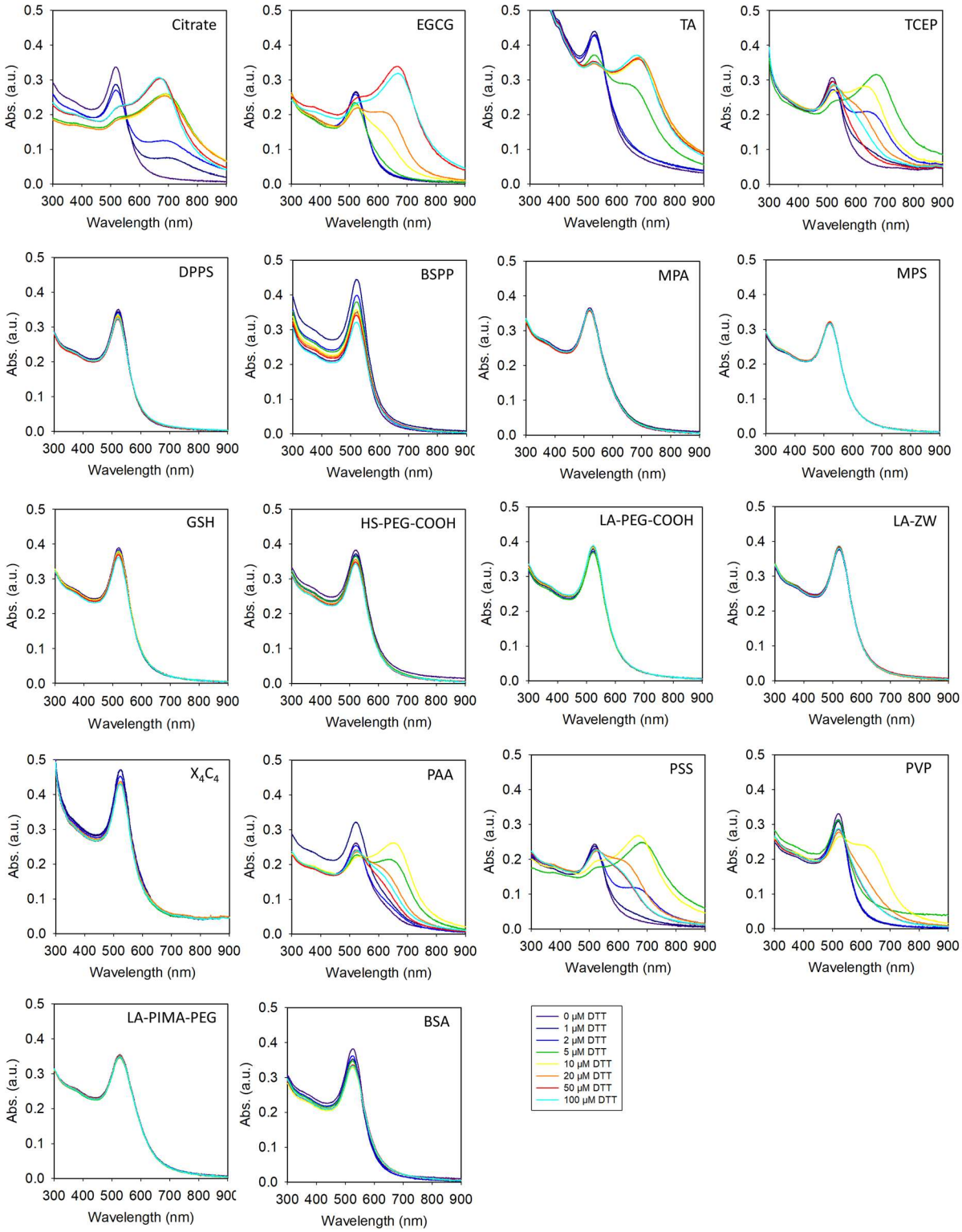

Figure S1.4. Absorption spectra of AuNPs capped with different ligands when incubated with various concentrations (0, 1, 2, 5, 10, 20, 50, and 100 μM) of dithiothreitol (DTT) solution for 10 minutes. Note that all the DTT solution contains 10 mM of NaCl to promote the covalent aggregation of AuNPs.

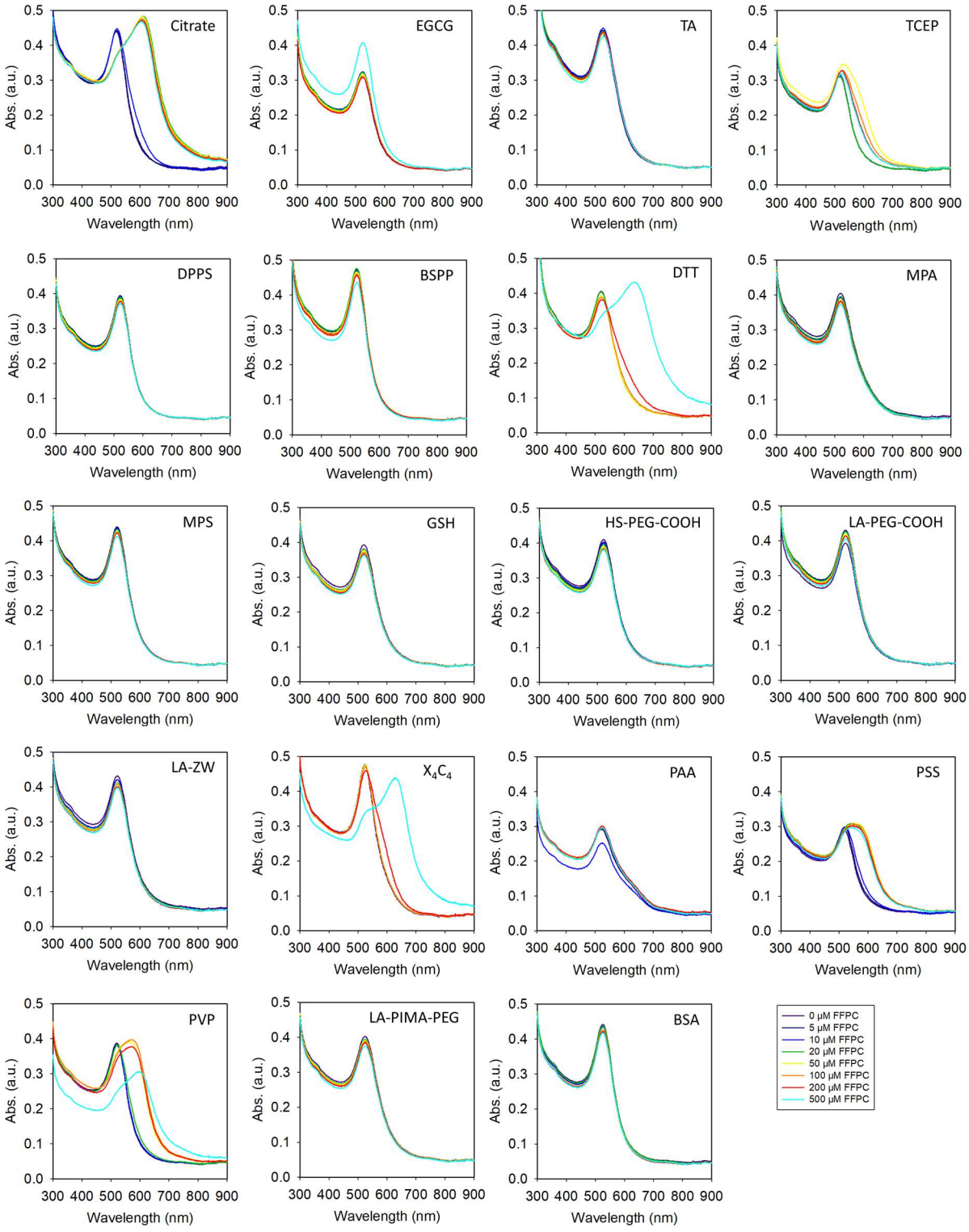

Figure S1.5. Absorption spectra of AuNPs capped with different ligands when incubated with various concentrations (0, 5, 10, 20, 50, 100, 200, and 500 μM) of amphiphilic FFPC peptide solution for 10 minutes.

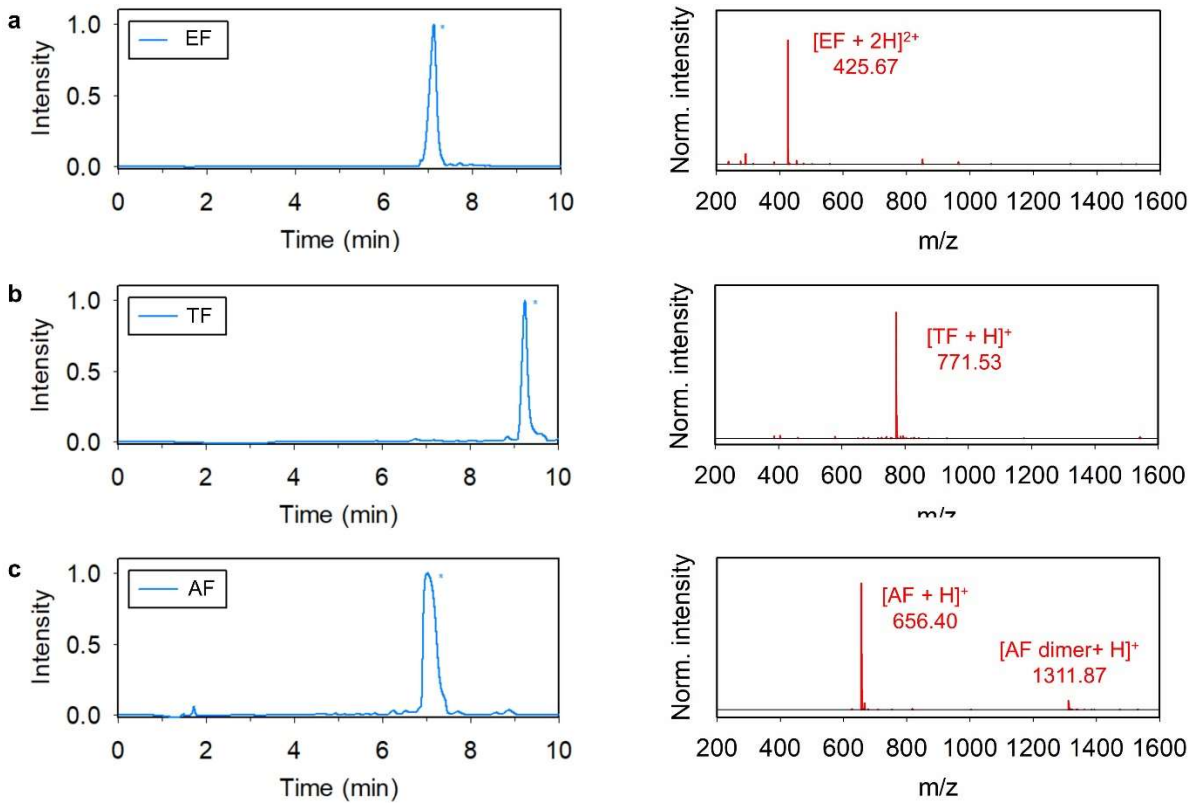

Figure S1.6. HPLC and ESI-MS data of the peptide segments including (a) EF, (b) TF, and (c) AF. The peptide information can be found in Table 2. $[EF+2H]^{2+}/2$ calcd. for 425.22; found, 425.67. $[TF+H]^{+}$ calcd. for 771.28; found, 771.53. [AF+H]+ calcd. for 656.28; found, 656.40.

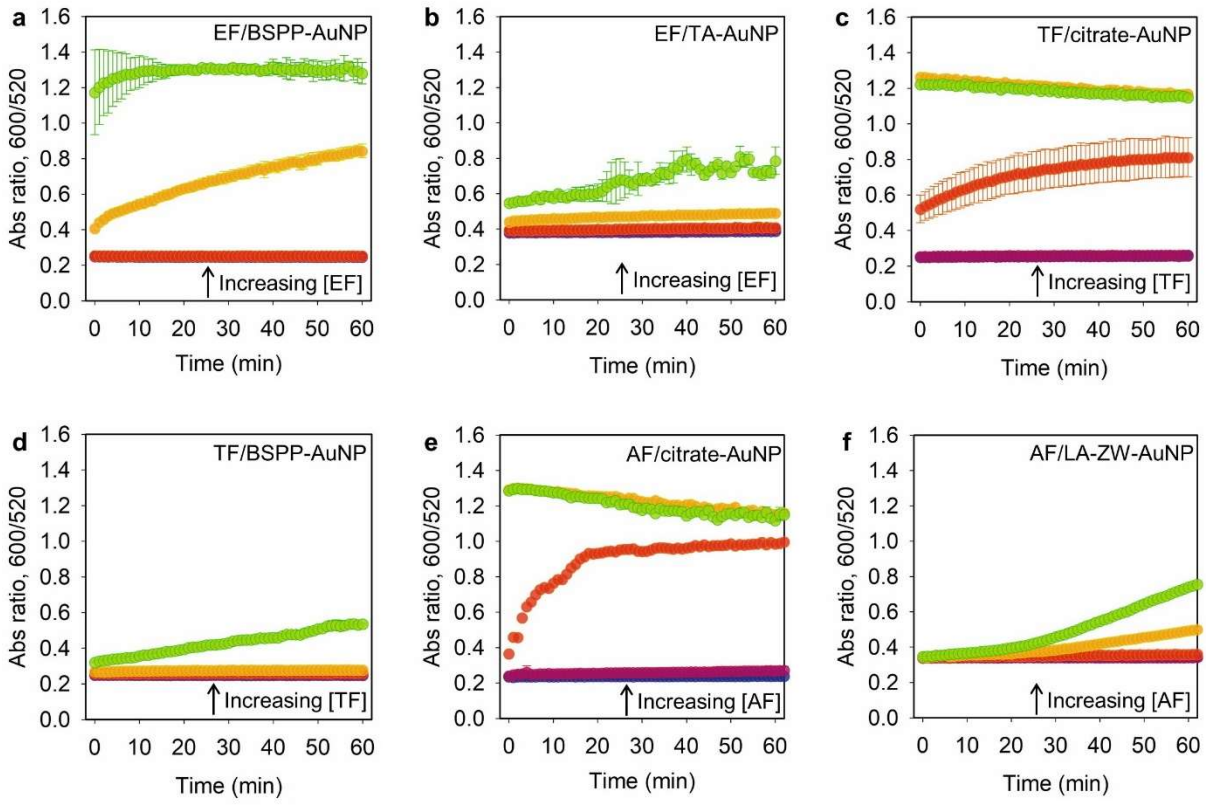

Figure S1.7. Time-dependent aggregation kinetics of the ligated AuNPs in the presence of peptide fragments for over 1 h. Absorbance ratio (Abs_{600}/Abs_{520}) of **(a)** EF peptide mixed with BSPP-AuNPs, **(b)** EF peptide mixed with tannic acid-AuNPs, **(c)** TF peptide mixed with citrate-AuNPs, and (d) TF peptide mixed with BSPP-AuNPs. **(e)** AF peptide mixed with citrate-AuNPs, and **(f)** AF peptide mixed with LA-ZW-AuNPs. Each plot shows five peptide concentrations from 0.1, 0.5, 2 (red), 10 (yellow), 50 (green) μM. Error bars = standard deviations (n = 3). The data points at 10 min were extracted for analyzing the critical coagulation concentration (CCC).

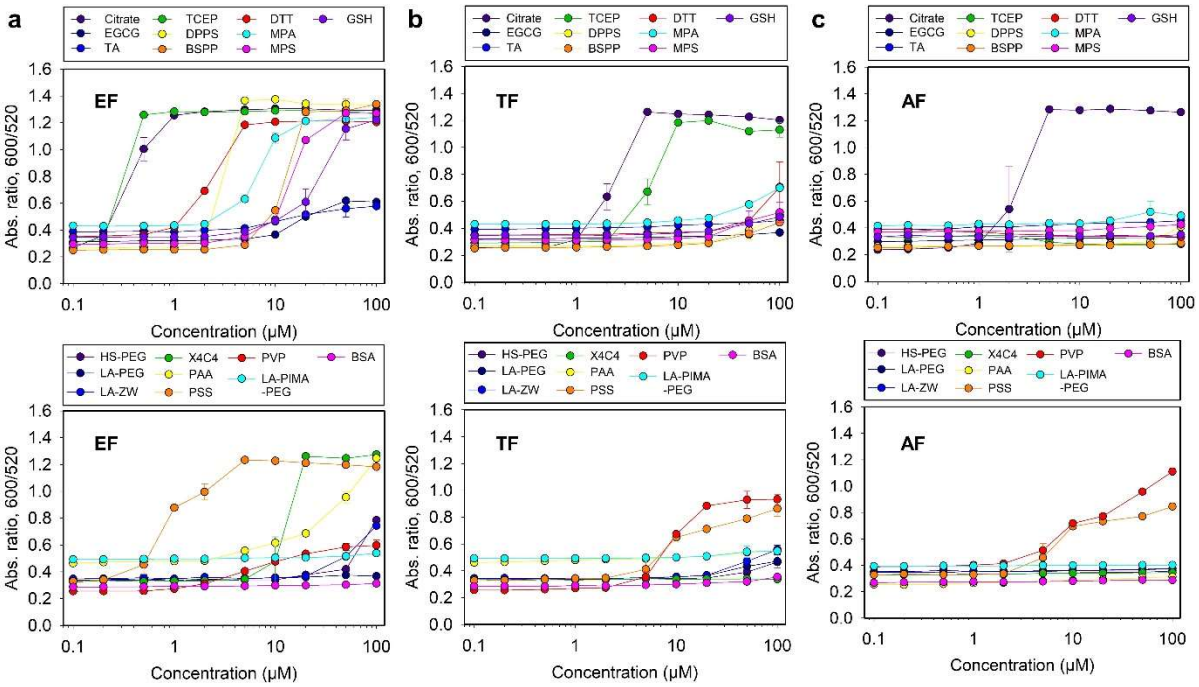

Figure S1.8. Concentration-dependent absorbance ratio (Abs600/Abs520) of the ligated AuNPs after incubating with the **(a)** EF, **(b)** TF, and **(c)** AF peptides for 10 minutes. The critical coagulation concentration (CCC) is defined as the first concentration of signal jump and is summarized in Table 1.3. The EF segment aggregates the AuNPs coated with citrate, EGCG, TA, TCEP, DPPS, BSPP, DTT, MPA, MPS, X4C4, PAA, and PSS molecules. The TF segment aggregates the AuNPs coated with citrate, TCEP, PVP, and PSS molecules. The AF segment aggregates the AuNPs coated with citrate, PVP, and PSS molecules.

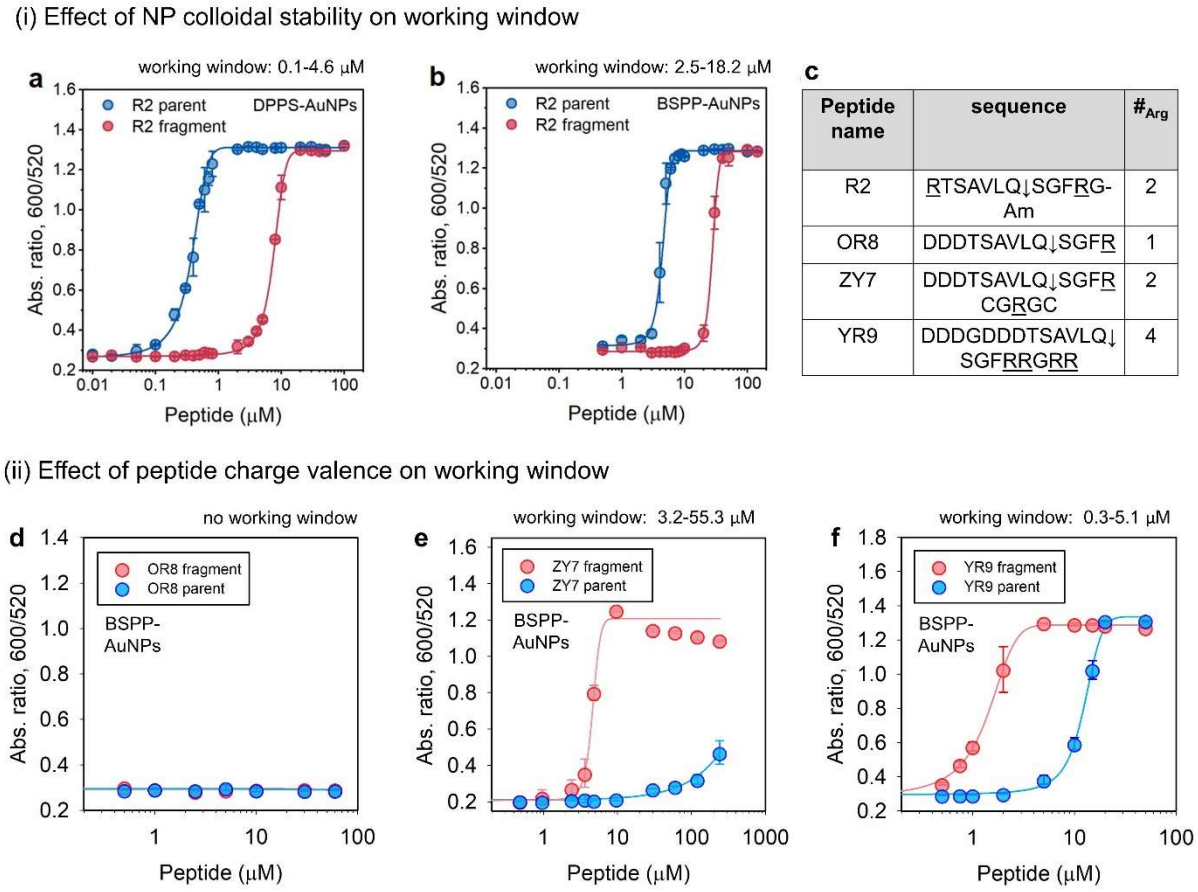

Peptide name	sequence	#$_{Arg}$
R2	RTSAVLQ↓SGFRG-Am	2
OR8	DDDTSAVLQ↓SGFR	1
ZY7	DDDTSAVLQ↓SGFR CGRGC	2
YR9	DDDGDDDTSAVLQ↓ SGFRRGRR	4

Figure S1.9. The choice of a peptide/AuNP pair as a good color sensor is determined by the charge valence of counterions and the matched colloidal stability. Working windows of Mpro sensors based on ratiometric signal (Abs_{600}/Abs_{520}) collected from **(a)** DPPS-AuNPs, and **(b)** BSPP-AuNPs incubated with various amounts of R2 parent (blue) and fragments (red), respectively. For peptide charge valence of 2 (i.e., R2 peptide), BSPP-AuNPs of higher colloidal stability showed a wider working window than that of the DPPS-AuNPs of weaker colloidal stability, e.g., 2.5-18.2 μM versus 0.1-4.6 μM.12 **(d)** When peptide of one positive charge valence [i.e., #Arg = 1 for OR8 peptide, sequence in DDDTSAVLQ↓SGFR] is combined use with BSPP-AuNPs, both parent and fragment could not induce aggregation due to the mismatched colloidal stability of BSPP-AuNPs, that is, effective working window does not exist. **(e)** When peptide of two positive charge valence [i.e., #Arg = 2 for ZY7 peptide, sequence in DDDTSAVLQ↓SGFRCGRGC] is combined use with BSPP-AuNPs, a large working window is resulted due to the matched colloidal stability of BSPP-AuNPs. **(f)** When peptide of four positive charge valence [i.e., #Arg = 4 for YR9 peptide, sequence in DDDGDDDTSAVLQ↓SGFRRGRR] is combined use with BSPP-AuNPs, a narrow-or-no effective working window is resulted due to the mismatched colloidal stability of BSPP-AuNPs. The peptide information is shown in panel c. The low and high limit of working window are determined. Panels a-b are reprinted with permission from ref. 12. Copyright (2023) Royal Society of Chemistry. Panels d-f are reprinted with permission from ref. 53. Copyright (2022) Wiley-VCH Verlag GmbH & Co. KGaA.

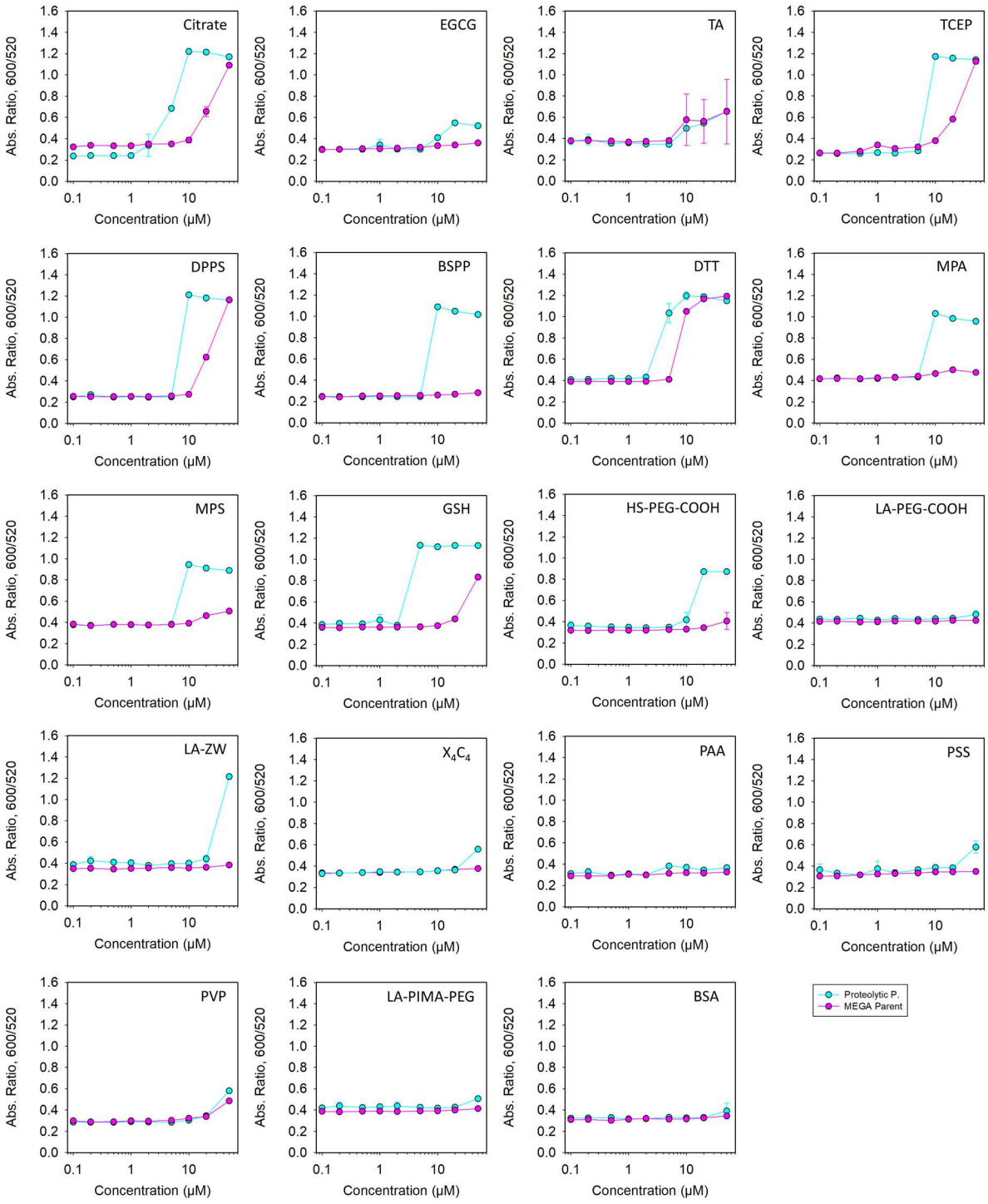

Figure S1.10. Working window of Mega peptide containing two Arg, Cys, and Phe residues with different ligated AuNPs. The parent peptide (purple curve) was incubated with M^{pro} at 37°C overnight to ensure that the peptide is fully cleaved (cyan curve). The AuNPs capped with citrate, DPPS, BSPP, MPA, MPS, GSH, HS-PEG-COOH, LA-ZW, X_4C_4, and PSS all have good sensing values.

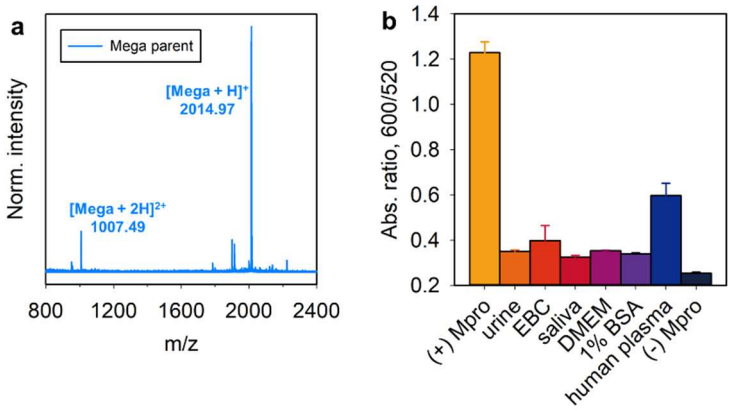

Figure S1.11. (a) ESI-MS data of intact Mega peptide. **(b)** The stability of BSPP-AuNPs (3.4 nM, 100 µL) in different matrix media (20 µL). Positive control used tris buffer with Mpro. The negative control used tris buffer without Mpro. The BSPP-AuNPs showed little color change in human plasma.

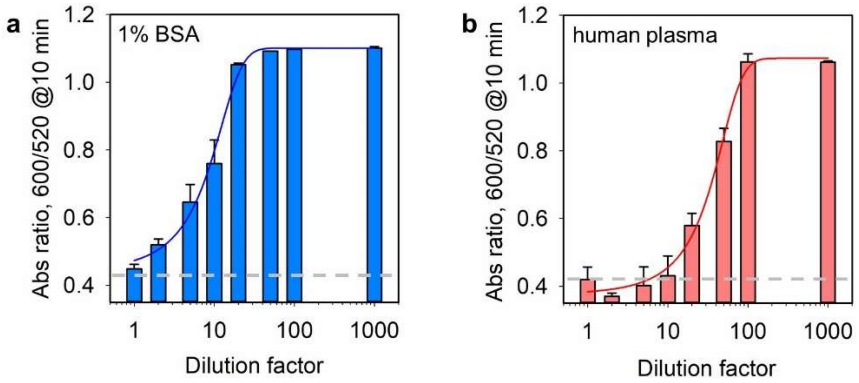

Figure S1.12. Dilution factor required for inducing color changes in **(a)** 1% w/v BSA and **(b)** human plasma. The dilution factors used 1×, 2×, 5×, 10×, 20×, 50×, 100×, and 1000×.The procedure follows the protocol in Section 8, Supporting Information, and Mega peptide (50 µM), Mpro (50 nM), and BSPP-AuNPs (3.4 nM, 100 µL) were used. A dilution factor of 5× is optimal for aggregation in 1% BSA, and a dilution factor of 20× is optimal for the human plasma matrix. The dash grey line indicates the base line where no aggregation or color change occurs.

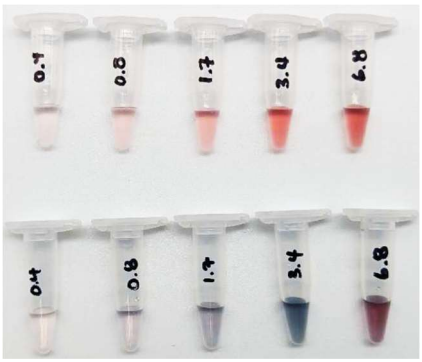

Figure S1.13. Concentration optimization of the 13-nm AuNPs for aggregation-based colorimetric assays. Citrate-AuNPs (100 μL) and NaCl (5 μL, 150 mM) were used for the experiments. The tested concentrations from left to right are 0.4, 0.8, 1.7, 3.4, and 6.8 nM. We chose 3.4 nM as the optimal NP concentration for the sake of reducing the amount of aggregants (or titrants) used for aggregation, while still giving intense and visible color changes.

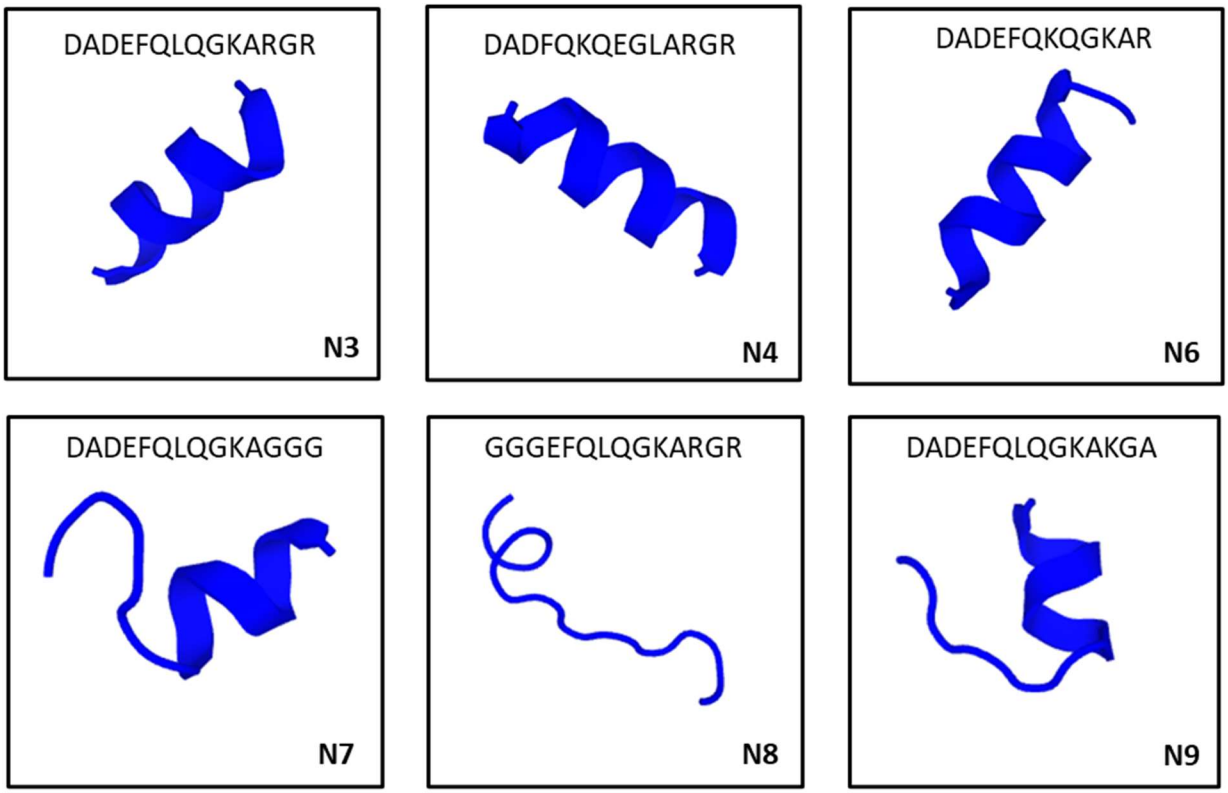

Figure S2.1. 3-D Computational folding images of peptide derivatives. Simulations of peptide folding were done using the publicly available PEP-FOLD 3 platform. The highest probable model for each peptide was reported. Observed structures include α-helixes, straight chains, and combinations thereof.

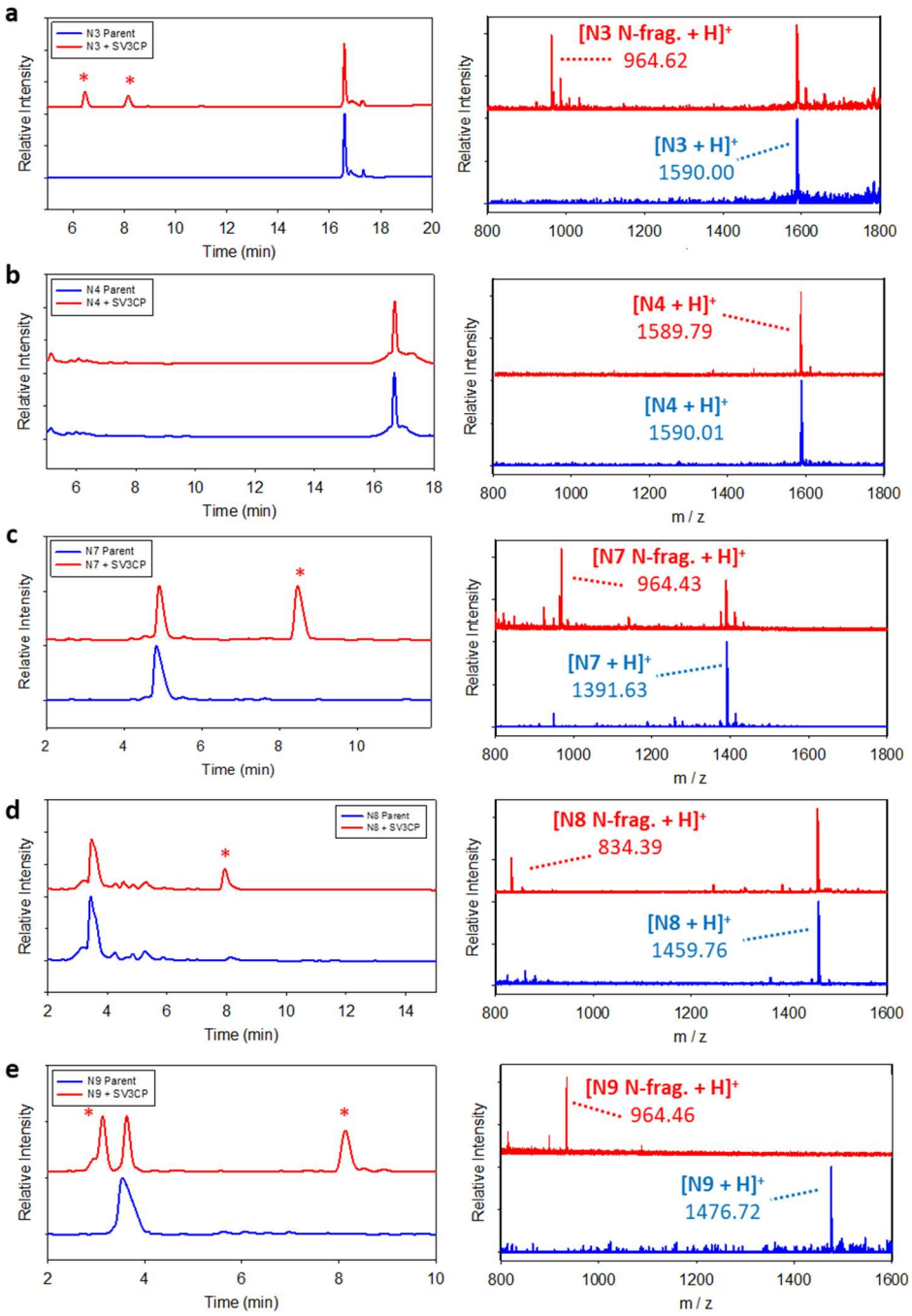

Figure S2.2. Confirmation of SV3CP-mediated cleavage of peptide derivatives. (left) HPLC before and after incubation with SV3CP and (right) MALDI-TOF MS before (blue) and after (red) incubation with SV3CP for pepeitdes (a) N3, (b) N4, (c) N7, (d) N8, and (e) N9. '*' denotes the presence of new peaks due to proteolysis. All peptides were incubated with SV3CP at a [E]:[S] ratio of 1:200 for 48 hours. Proteolysis is confirmed through the detection of the N-fragment. Note, MALDI-TOF MS analysis of the cleavage was conducted on the crude proteolysis reaction; mass spectrometry of individual HPLC peaks was not suitable due to the fractions having low yields.

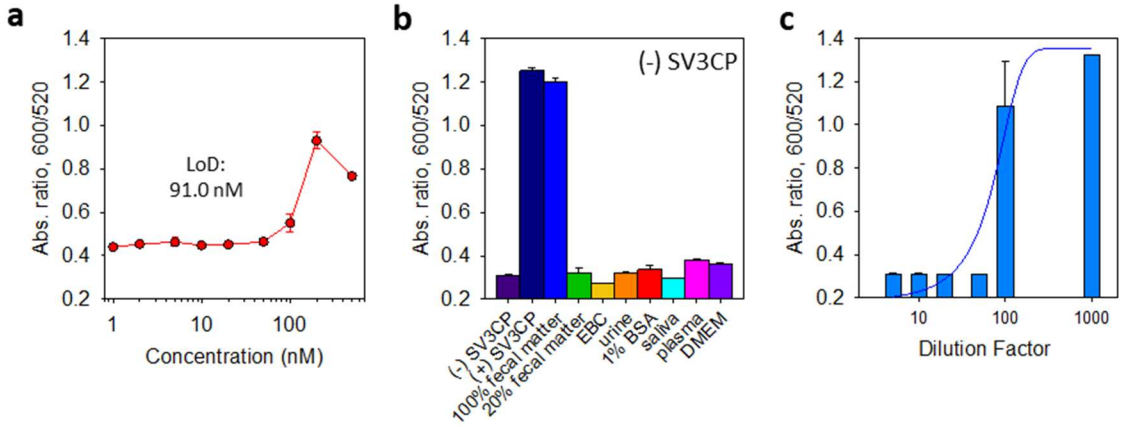

Figure S2.3. Limit of detection of SV3CP after 8 hours, nanoparticle colloidal stability in biological matrices, and fecal matter dilutions. (a) Ratiometric absorbance as a function of SV3CP concentration. N6 substrate (50 µM) and BSPP-AuNPs (3.4 nM) were employed. The substrate was incubated with the protease in TB buffer for 8 hours before addition of BSPP-AuNPs. (b) Ratiometric absorbance of BSPP-AuNPs (3.4 nM, 100 µL) in various biological matrices (20 µL). Particles were colloidally stable in all matrices except fecal matter, which required a minimum 1 in 5 dilution to prevent aggregation. (-) and (+) SV3CP in TB buffer were included as negative and positive controls respectively. (c) Ratiometric absorbance as a function of dilutions of fecal matter matrix. Fecal matter matrix was prepared by vortexing 100 mg of human feces in 1.5 mL of TB buffer for 4 minutes and centrifuging the resulting mixture at 20 XG for 15 seconds. The supernatant is taken and passed through a 50 kDa filter to produce the final product. A minimum dilution factor of 5 is needed to prevent matrix-induced aggregation of the AuNPs. 100 nM of SV3CP is then incubated with the N6 substrate in varying dilution factors of fecal matter matrix (e.g., 5 – 1000) in 20 µL for 48 hours, followed by addition of BSPP-AuNPs (3.4 nM, 100 µL) for colorimetric readout.

Critical coagulation concentration (CCC) calculation:

$$\mathrm{CCC} \equiv \mathrm{LoD_{int.}} = \mathrm{mean_{blank}} + 1.645 \times (\mathrm{SD_{blank}}) + 1.645 \times (\mathrm{SD_{low\ conc.\ sample}}) \tag{S2.1}$$

Enzyme kinetics for fluorogenic substrate:

$$\mathrm{E} + \mathrm{S} \underset{\mathrm{k_{off}}}{\overset{\mathrm{k_{on}}}{\rightleftharpoons}} \mathrm{ES} \underset{k_{-ca}}{\overset{\mathrm{k_{cat}}}{\rightleftharpoons}} \mathrm{E} + \mathrm{P} \tag{S2.2}$$

$$\upsilon = \frac{\upsilon_{max}}{K_M + [S]_0} \tag{S2.3}$$

REFERENCES

1. M. Song, D. Wang, S. Peana, S. Choudhury, P. Nyga, Z. A. Kudyshev, H. Yu, A. Boltasseva, V. M. Shalaev and A. V. Kildishev, *Appl. Phys. Rev.*, 2019, **6**, 041308.

2. M. Grzelczak, L. M. Liz-Marzán and R. Klajn, *Chem. Soc. Rev.*, 2019, **48**, 1342.

3. P. Chen, X. Liu, G. Goyal, N. T. Tran, J. C. Shing Ho, Y. Wang, D. Aili and B. Liedberg, *Anal. Chem.*, 2018, **90**, 4916.

4. J. Zeng, Y. Zhang, T. Zeng, R. Aleisa, Z. Qiu, Y. Chen, J. Huang, D. Wang, Z. Yan and Y. Yin, *Nano Today*, 2020, **32**, 100855.

5. M. Retout, Y. Mantri, Z. Jin, J. Zhou, G. Noël, B. Donovan, W. Yim and J. V. Jokerst, *ACS Nano*, 2022, **16**, 6165.

6. M. Retout, Z. Jin, J. Tsujimoto, Y. Mantri, R. Borum, M. N. Creyer, W. Yim, T. He, Y. C. Chang and J. V. Jokerst, *ACS Appl. Mater. Interfaces*, 2022, **14**, 52553.

7. V. Jain, S. Roy, P. Roy and P. P. Pillai, *Chem. Mater.*, 2022, **34**, 7579.

8. A. Heuer-Jungemann, N. Feliu, I. Bakaimi, M. Hamaly, A. Alkilany, I. Chakraborty, A. Masood, M. F. Casula, A. Kostopoulou, E. Oh, K. Susumu, M. H. Stewart, I. L. Medintz, E. Stratakis, W. J. Parak and A. G. Kanaras, *Chem. Rev.*, 2019, **119**, 4819.

9. W. Zhou, X. Gao, D. Liu and X. Chen, *Chem. Rev.*, 2015, **115**, 10575.

10. K. Saha, S. S. Agasti, C. Kim, X. Li and V. M. Rotello, *Chem. Rev.*, 2012, **112**, 2739.

11. L. Polavarapu, J. Pérez-Juste, Q. H. Xu and L. M. Liz-Marzán, *J. Mater. Chem. C*, 2014, **2**, 7460.

12. P. D. Howes, R. Chandrawati and M. M. Stevens, *Science*, 2014, **346**, 1247390.

13. H. Aldewachi, T. Chalati, M. N. Woodroofe, N. Bricklebank, B. Sharrack and P. Gardiner, *Nanoscale*, 2018, **10**, 18.

14. M. Alafeef and D. Pan, *ACS Nano*, 2022, **16**, 11545.

15. Z. Jin, J. Yeung, J. Zhou, Y. Cheng, Y. Li, Y. Mantri, T. He, W. Yim, M. Xu, Z. Wu, P. Fajtova, M. N. Creyer, C. Moore, L. Fu, W. F. Penny, A. J. O'Donoghue and J. V. Jokerst, *Chem. Mater.*, 2022, **34**, 1259.

16. C. Guarise, L. Pasquato, V. De Filippis and P. Scrimin, *Proc. Natl. Acad. Sci. U.S.A.*, 2006, **103**, 3978.

17. D. Ye, A. J. Shuhendler, L. Cui, L. Tong, S. S. Tee, G. Tikhomirov, D. W. Felsher and J. Rao, *Nat. Chem.*, 2014, **6**, 519.

18. C. A. Mirkin, R. L. Letsinger, R. C. Mucic and J. J. Storhoff, *Nature*, 1996, **382**, 607.

19. C. N. Loynachan, A. P. Soleimany, J. S. Dudani, Y. Lin, A. Najer, A. Bekdemir, Q. Chen, S. N. Bhatia and M. M. Stevens, *Nat. Nanotechnol.*, 2019, **14**, 883.

20. T. Bian, A. Gardin, J. Gemen, L. Houben, C. Perego, B. Lee, N. Elad, Z. Chu, G. M. Pavan and R. Klajn, *Nat. Chem.*, 2021, **13**, 940.

21. R. M. Choueiri, A. Klinkova, H. Thérien-Aubin, M. Rubinstein and E. Kumacheva, *J. Am. Chem. Soc.*, 2013, **135**, 10262.

22. P. K. Kundu, D. Samanta, R. Leizrowice, B. Margulis, H. Zhao, M. Börner, T. Udayabhaskararao, D. Manna and R. Klajn, *Nat. Chem.*, 2015, **7**, 646.

23. Z. Jin, Y. Mantri, M. Retout, Y. Cheng, J. Zhou, A. Jorns, P. Fajtova, W. Yim, C. Moore, M. Xu, M. N. Creyer, R. M. Borum, J. Zhou, Z. Wu, T. He, W. F. Penny, A. J. O'Donoghue and J. V. Jokerst, *Angew. Chem., Int. Ed.*, 2022, **61**, e202112995.

24. Z. Jin, C. Ling, Y. Li, J. Zhou, K. Li, W. Yim, J. Yeung, Y. C. Chang, T. He, Y. Cheng, P. Fajtová, M. Retout, A. J. O'Donoghue and J. V. Jokerst, *Nano Lett.*, 2022, **22**, 8932.

25. Z. Jin, Y. Li, K. Li, J. Zhou, J. Yeung, C. Ling, W. Yim, T. He, Y. Cheng, M. Xu, M. N. Creyer, Y. C. Chang, P. Fajtová, M. Retout, B. Qi, S. Li, A. J. O'Donoghue and J. V. Jokerst, *Angew. Chem.*, 2023, **135**, e202214394.

26. M. N. Creyer, Z. Jin, C. Moore, W. Yim, J. Zhou and J. V. Jokerst, *ACS Appl. Mater. Interfaces*, 2021, **13**, 45236.

27. R. Wu, L. P. Jiang, J. J. Zhu and J. Liu, *Langmuir*, 2019, **35**, 13461.

28. K. H. Su, Q. H. Wei, X. Zhang, J. J. Mock, D. R. Smith and S. Schultz, *Nano Lett.*, 2003, **3**, 1087.

29. Z. Jin, Y. Sugiyama, C. Zhang, G. Palui, Y. Xin, L. Du, S. Wang, N. Dridi and H. Mattoussi, *Chem. Mater.*, 2020, **32**, 7469.

30. M. V. Kovalenko, M. I. Bodnarchuk, J. Zaumseil, J. S. Lee and D. V. Talapin, *J. Am. Chem. Soc.*, 2010, **132**, 10085.

31. G. Palui, F. Aldeek, W. Wang and H. Mattoussi, *Chem. Soc. Rev.*, 2015, **44**, 193.

32. J. V. Jokerst, T. Lobovkina, R. N. Zare and S. S. Gambhir, *Nanomedicine*, 2011, **6**, 715.

33. E. A. Egorova, M. M. J. van Rijt, N. Sommerdijk, G. S. Gooris, J. A. Bouwstra, A. L. Boyle and A. Kros, *ACS Nano*, 2020, **14**, 5874.

34. B. Stordy, Y. Zhang, Z. Sepahi, M. H. Khatami, P. M. Kim and W. C. W. Chan, *Chem. Mater.*, 2022, **34**, 6868.

35. H. Ohshima, *Electrical Phenomena at Interfaces and Biointerfaces*, 2012.

36. X. Liu, Q. Zhang, W. Knoll, B. Liedberg and Y. Wang, *Adv. Mater.*, 2020, **32**, 2000866.

37. A. Laromaine, L. Koh, M. Murugesan, R. V. Ulijn and M. M. Stevens, *J. Am. Chem. Soc.*, 2007, **129**, 4156.

38. Y. Yang, H. Qin, M. Jiang, L. Lin, T. Fu, X. Dai, Z. Zhang, Y. Niu, H. Cao, Y. Jin, F. Zhao and X. Peng, *Nano Lett.*, 2016, **16**, 2133.

39. B. C. Mei, E. Oh, K. Susumu, D. Farrell, T. J. Mountziaris and H. Mattoussi, *Langmuir*, 2009, **25**, 10604.

40. L. Troian-Gautier, A. Mattiuzzi, O. Reinaud, C. Lagrost and I. Jabin, *Org. Biomol. Chem.*, 2020, **18**, 3624.

41. R. G. Pearson, *Inorg. Chem.*, 1988, **27**, 734.

42. D. Wu, J. Zhou, M. N. Creyer, W. Yim, Z. Chen, P. B. Messersmith and J. V. Jokerst, *Chem. Soc. Rev.*, 2021, **50**, 4432.

43. H. Häkkinen, *Nat. Chem.*, 2012, **4**, 443.

44. A. O. Borissova, A. A. Korlyukov, M. Y. Antipin and K. A. Lyssenko, *J. Phys. Chem. A*, 2008, **112**, 11519.

45. A. Antušek, M. Blaško, M. Urban, P. Noga, D. Kisić, M. Nenadović, D. Lončarević and Z. Rakočević, *Phys. Chem. Chem. Phys.*, 2017, **19**, 28897.

46. D. H. Tsai, T. J. Cho, F. W. DelRio, J. M. Gorham, J. Zheng, J. Tan, M. R. Zachariah and V. A. Hackley, *Langmuir*, 2014, **30**, 3397.

47. M. Retout, I. Jabin and G. Bruylants, *ACS Omega*, 2021, **6**, 19675.

48. C. Zhang, Z. Jin, B. Zeng, W. Wang, G. Palui and H. Mattoussi, *J. Phys. Chem. B*, 2020, **124**, 4631.

49. B. D. Johnston, W. G. Kreyling, C. Pfeiffer, M. Schäffler, H. Sarioglu, S. Ristig, S. Hirn, N. Haberl and W. J. Parak, *Adv. Funct. Mater.*, 2017, **27**, 1701956.

50. J. Mosquera, I. García, M. Henriksen-Lacey, G. González-Rubio and L. M. Liz-Marzán, *Chem. Mater.*, 2019, **31**, 57.

51. K. Susumu, B. C. Mei and H. Mattoussi, *Nat. Protoc.*, 2009, **4**, 424.

52. S. Bera, S. Mondal, B. Xue, L. J. W. Shimon, Y. Cao and E. Gazit, *Nat. Mater.*, 2019, **18**, 503.

53. Y. C. Chang, Z. Jin, K. Li, J. Zhou, W. Yim, J. Yeung, Y. Cheng, M. Retout, M. N. Creyer, P. Fajtová, T. He, X. Chen, A. J. O'Donoghue and J. V. Jokerst, *Chem. Sci.*, 2023, **14**, 2659.

54. D. A. Armbruster and T. Pry, *Clin. Biochem. Rev.*, 2008, **29**, S49.

55. B. Graham, T. L. Bailey, J. R. J. Healey, M. Marcellini, S. Deville and M. I. Gibson, *Angew. Chem., Int. Ed.*, 2017, **56**, 15941.

56. Y. Cheng, R. M. Borum, A. E. Clark, Z. Jin, C. Moore, P. Fajtová, A. J. O'Donoghue, A. F. Carlin and J. V. Jokerst, *Angew. Chem., Int. Ed.*, 2022, **61**, e202113617.

57. S. Sokalingam, G. Raghunathan, N. Soundrarajan and S. G. Lee, *PLoS One*, 2012, **7**, e40410.

58. P. Martínez-Fleta, A. Alfranca, I. González-Álvaro, J. M. Casasnovas, D. Fernández-Soto, G. Esteso, Y. Cáceres-Martell, S. Gardeta, C. López-Sanz and M. Valés-Gómez, *J. Immunol. Res.*, 2020, **205**, 3130.

59. Y. Feng, G. Liu, M. La and L. Liu, *Molecules*, 2022, **27**, 615.

60. C. Moore, R. M. Borum, Y. Mantri, M. Xu, P. Fajtová, A. J. O'Donoghue and J. V. Jokerst, *ACS Sens.*, 2021, **6**, 2356.

61. J. Vandooren and Y. Itoh, *Front. Immunol.*, 2021, **12**, 803244.

62. J. Wang, S. w. Hsu, N. Gonzalez-Pech, A. Jhunjhunwala, F. Chen, A. Hariri, V. Grassian, A. Tao and J. V. Jokerst, *Part. Part. Syst. Charact.*, 2019, **36**, 1900171.

63. Z. Jin, A. Kapur, W. Wang, J. D. Hernandez, M. Thakur and H. Mattoussi, *J. Chem. Phys.*, 2019, **151**, 164703.

64. W. E. Kaman, F. Galassi, J. J. de Soet, S. Bizzarro, B. G. Loos, E. C. Veerman, A. van Belkum, J. P. Hays and F. J. Bikker, *J. Clin. Microbiol.*, 2012, **50**, 104.

65. P. R. Lambden, E. O. Caul, C. R. Ashley, I. N. Clarke and *Science*, 1993, **259**, 516-519.

66. A. J. Hall, J. Vinjé, B. Lopman, G. W. Park, C. Yen, N. Gregoricus, U. Parashar and *Morbidity and Mortality Weekly Report: Recommendations and Reports*, 2011, **60**, 1-15.

67. M. A. Argudin, M. C. Mendoza and M. R. Rodicio, *Toxins (Basel)*, 2010, **2**, 1751-1773.

68. M. R. Herod, C. A. Prince, R. J. Skilton, V. K. Ward, J. B. Cooper, I. N. Clarke and *Biochemical Journal*, 2014, **464**, 461-472.

69. G. Capece, E. Gignac and in *StatPearls*, Treasure Island (FL), 2022, DOI: 10.1007/978-3-030-27209-8.

70. Z. Jin, J. Yeung, J. Zhou, M. Retout, W. Yim, P. Fajtová, B. Gosselin, I. Jabin, G. Bruylants, H. Mattoussi, A. J. O'Donoghue, J. V. Jokerst and *ACS Applied Materials & Interfaces*, 2023, **15**, 20483-20494.

71. M. De Graaf, J. Van Beek, M. P. G. Koopmans and *Nature Reviews Microbiology*, 2016, **14**, 421-433.

72. G. Sener, L. Uzun, A. Denizli and *ACS Applied Materials and Interfaces*, 2014, **6**, 18395-18400.

73. J. Chen, Y. Ma, W. Du, T. Dai, Y. Wang, W. Jiang, Y. Wan, Y. Wang, G. Liang, G. Wang and *Advanced Functional Materials*, 2020, **30**, 2001566.

74. J. Guo, A. Douangamath, W. Song, A. R. Coker, A. W. E. Chan, S. P. Wood, J. B. Cooper, E. Resnick, N. London, F. v. Delft and *Journal of Structural Biology: X*, 2020, **4**, 100031.

75. M. Yon, C. Pibourret, J. D. Marty, D. Ciuculescu-Pradines and *Nanoscale Advances*, 2020, **2**, 4671-4681.

76. I. André, S. Linse, F. A. A. Mulder and *Journal of the American Chemical Society*, 2007, **129**, 15805-15813.

77. K. J. Cutrona, B. A. Kaufman, D. M. Figueroa and D. E. Elmore, *FEBS Lett*, 2015, **589**, 3915-3920.

78. C. Dardonville, B. A. Caine, M. Navarro De La Fuente, G. Martín Herranz, B. Corrales Mariblanca, P. L. A. Popelier and *New Journal of Chemistry*, 2017, **41**, 11016-11028.

79. M. Vazdar, J. Heyda, P. E. Mason, G. Tesei, C. Allolio, M. Lund, P. Jungwirth and *Accounts of Chemical Research*, 2018, **51**, 1455-1464.

80. P. Viswanathan, J. May, S. Uhm, C. Yon, B. Korba and *Virology*, 2013, **438**, 20-27.

81. K. O. Chang, D. Takahashi, O. Prakash, Y. Kim and *Virology*, 2012, **423**, 125-133.

82. Z. Jin, A. Jorns, W. Yim, R. Wing, Y. Mantri, J. Zhou, J. Zhou, Z. Wu, C. Moore, W. F. Penny, J. V. Jokerst and *Analytical Chemistry*, 2021, **93**, 11025-11032.

83. A. Hellysaz, M. Neijd, T. Vesikari, L. Svensson, M. Hagbom, V. R. Prasad, A. Einstein and *mBio*, 2023, **14**.

84. J. M. Jung, G. Savin, M. Pouzot, C. Schmitt, R. Mezzenga and *Biomacromolecules*, 2008, **9**, 2477-2486.

85. D. R. Colquhoun, K. J. Schwab, R. N. Cole, R. U. Halden and *Applied and Environmental Microbiology*, 2006, **72**, 2749.

86. G. Tung-Thompson, D. A. Libera, K. L. Koch, F. L. De Los Reyes, L. A. Jaykus and *PLoS ONE*, 2015, **10**.

87. V. Nemeth and N. Pfleghaar, in *StatPearls*, Treasure Island (FL), 2023.

88. L. Monteiro, D. Bonnemaison, A. Vekris, K. G. Petry, J. Bonnet, R. Vidal, J. Cabrita, F. Mégraud and *Journal of Clinical Microbiology*, 1997, **35**, 995-998.

89. R. Rampado, S. Crotti, P. Caliceti, S. Pucciarelli, M. Agostini and *Frontiers in Bioengineering and Biotechnology*, 2020, **8**, 166.

90. J. Vinjé and *Journal of Clinical Microbiology*, 2015, **53**, 373-381.